






The Companion Mass Distribution of Post Common Envelope Hot Subdwarf Binaries: Evidence for Boosted and Disrupted Magnetic Braking?

Lisa Blomberg¹ , Kareem El-Badry¹, Katelyn Breivik², Ilaria Caiazzo³, Pranav Nagarajan¹ , Antonio Rodriguez¹,
Jan van Roestel⁴, Zachary P. Vanderbosch¹, and Natsuko Yamaguchi¹ 

¹Department of Astronomy, California Institute of Technology, 1200 East California Boulevard, Pasadena, CA 91125, USA

²McWilliams Center for Cosmology, Department of Physics, Carnegie Mellon University, Pittsburgh, PA 15213, USA

³Institute of Science and Technology Austria, Am Campus 1, 3400 Klosterneuburg, Austria

⁴Anton Pannekoek Institute for Astronomy, University of Amsterdam, 1090 GE Amsterdam, The Netherlands

Received 2024 August 23; accepted 2024 November 19; published 2024 December 13

Abstract

We measure the mass distribution of main-sequence (MS) companions to hot subdwarf B stars (sdBs) in post-common envelope binaries (PCEBs). We carried out a spectroscopic survey of 14 eclipsing systems (“HW Vir binaries”) with orbital periods of $3.8 < P_{\text{orb}} < 12$ hr, resulting in a well-understood selection function and a near-complete sample of HW Vir binaries with $G < 16$. We constrain companion masses from the radial velocity curves of the sdB stars. The companion mass distribution peaks at $M_{\text{MS}} \approx 0.15 M_{\odot}$ and drops off at $M_{\text{MS}} > 0.2 M_{\odot}$, with only two systems hosting companions above the fully convective limit. There is no correlation between P_{orb} and M_{MS} within the sample. A similar drop-off in the companion mass distribution of white dwarf (WD) + MS PCEBs has been attributed to disrupted magnetic braking (MB) below the fully convective limit. We compare the sdB companion mass distribution to predictions of binary evolution simulations with a range of MB laws. Because sdBs have short lifetimes compared to WDs, explaining the lack of higher-mass MS companions to sdBs with disrupted MB requires MB to be boosted by a factor of 20–100 relative to MB laws inferred from the rotation evolution of single stars. We speculate that such boosting may be a result of irradiation-driven enhancement of the MS stars’ winds. An alternative possibility is that common envelope evolution favors low-mass companions in short-period orbits, but the existence of massive WD companions to sdBs with similar periods disfavors this scenario.

Unified Astronomy Thesaurus concepts: [B subdwarf stars \(129\)](#); [Common envelope binary stars \(2156\)](#); [Eclipsing binary stars \(444\)](#); [Multiple star evolution \(2153\)](#)

1. Introduction

Magnetic braking (MB) is one of the primary drivers of angular momentum loss in binaries. Magnetic fields cause mass lost in a stellar wind to co-rotate with the star, such that the angular momentum of the wind is greater than that of the stellar surface. Over time, this removes angular momentum and causes the star to spin down (e.g., Schatzman 1962; Weber & Davis 1967; Mestel 1968; Mestel & Spruit 1987).

However, in close binaries, tides synchronize the component stars’ rotation with the orbital period (e.g., Zahn 1977). As a result, MB is not able to spin down either of the components. Instead, the wind removes angular momentum from the orbit, causing it to shrink and the components to spin up. This process plays a critical role in the evolution of close binaries: it brings detached binaries into contact and sets the period evolution and mass transfer rates of mass-transfer binaries, such as cataclysmic variables (e.g., Knigge et al. 2011). However, MB is imperfectly

understood theoretically. Most MB models used in binary evolution calculations are empirically calibrated from observations of the spin evolution of single stars (e.g., Skumanich 1972; Matt et al. 2015), most of which rotate slower than the stars in close, tidally locked binaries.

The MB prescription most widely used in the binary evolution literature is the model proposed by Verbunt & Zwaan (1981) and refined by Rappaport et al. (1983, hereafter RVJ). This model predicts a MB torque that scales as P_{orb}^{-3} , leading to accelerated inspiral at short periods. A key feature of this model is the prediction that MB is “disrupted” when a star becomes fully convective. This disruption was proposed to explain the “period gap” in the orbital period distribution of cataclysmic variables (CVs) at 2–3 hr, corresponding to donor masses near the fully convective boundary. In the disrupted magnetic braking (DMB) paradigm, this gap occurs because MB abruptly weakens when CV donors become fully convective, causing the donors to return to thermal equilibrium and temporarily halting mass transfer.

In support of the DMB model, it has been observed that the mass distribution of the main sequence (MS) stars in close

detached white dwarf (WD) + MS binaries peaks near $\sim 0.3M_{\odot}$ and falls off steeply at higher masses. A seminal study by Schreiber et al. (2010) carried out multi-epoch radial velocity (RV) follow-up on the published sample of WD + MS binaries from the Sloan Digital Sky Survey (SDSS; Rebassa-Mansergas et al. 2010). Politano & Weiler (2006) had previously proposed a test of the DMB paradigm based on the post common envelope binary (PCEB) companion mass distribution, predicting that the fraction of PCEBs relative to wide WD + MS binaries should decrease by 37%–73% above $M_{\text{MS}} \sim 0.37M_{\odot}$, which was their estimate of the fully convective limit. This drop is predicted because in the DMB paradigm, PCEBs with MS stars above the fully convective limit undergo MB-driven orbital inspiral and come into contact faster than PCEBs with fully convective MS stars. Schreiber et al. (2010) measured an 80% drop in the fraction of PCEBs above $M_{\text{MS}} \sim 0.3M_{\odot}$, interpreting this as evidence of DMB. As we discuss below, significant uncertainties in the MB law and its role in driving orbital evolution of PCEBs remain, motivating us to revisit the PCEB test of the DMB model.

Several results suggest that MB in low-mass stars may be more complex than suggested by the RVJ model. First, studies of the rotational evolution of single low-mass stars in clusters have found spin rates to vary with age in a manner that cannot be explained with simple prescriptions depending only on the structural parameters of the stars (e.g., Brown 2014; Newton et al. 2016; Bouma et al. 2023). In fact, some studies have even reported evidence for an increase in MB below the fully convective limit (Lu et al. 2024). Second, there is now a large body of evidence that MB torques do not scale as P_{orb}^{-3} at arbitrarily fast rotation rates, but instead saturate above a critical rotation rate corresponding to periods of order 10 days and thereafter have a shallower scaling with P_{orb} (e.g., Reiners et al. 2009; Matt et al. 2015; El-Badry et al. 2022). Third, several studies have proposed that CVs experience additional angular momentum losses as a consequence of the mass transfer process, in addition to those associated with MB (e.g., Schreiber et al. 2010).

Recently, Belloni et al. (2024) investigated whether a saturated MB model—which predicts that MB torques saturated above a critical rotation rate and is more consistent with observations of the rotation evolution of single stars and with the period distribution of detached MS + MS binaries—could also explain the companion mass distribution in the SDSS WD + MS PCEB sample when combined with disruption of MB below the fully convective limit. They found that it could, but only if the MB torque is at least ~ 50 times stronger than predicted by the models calibrated to single-star rotation rates.

While Schreiber et al. (2010) and Belloni et al. (2024) showed that the mass distribution of MS stars in WD + MS PCEBs could be explained as a result of MB, this may not be the only possible explanation, since the initial mass distribution of PCEBs directly after common envelope is uncertain.

In this paper, we investigate the companion mass distribution of another population of PCEBs: those containing a stripped core helium burning star (an “sdB,” e.g., Heber 2016) and a MS star. We focus on eclipsing systems, also known as HW Vir binaries. Close sdB + MS binaries are formed when a binary containing a red giant and a MS star undergoes a common envelope event during or shortly before the giant’s core helium flash. If the MS star’s orbital inspiral releases enough energy to eject the envelope, we are left with a detached binary comprised of a naked helium-burning star (i.e., the sdB) and a MS star. Close sdB + MS binaries thus form through a very similar process to WD + MS PCEBs. The key difference are that (a) the common envelope interaction in sdB + MS binaries must have occurred near the tip of the giant branch (e.g., Han et al. 2002) and (b) it must have occurred relatively recently, since sdB stars only live for about 100 Myr (Dorman et al. 1993; Schindler et al. 2015). Thus, there is less time for MB to shrink the orbit during the lifetime of the sdB, and we expect the period and mass distribution of sdB + MS binaries to more closely reflect the distribution immediately after common envelope.

If the observed lack of MS stars above the fully convective limit in WD + MS binaries is a result of DMB, we should expect a weaker drop-off toward higher masses in the mass distribution of sdB companions. Our basic approach is to measure the companion mass distribution of an observed sample of sdB + MS binaries with a well-understood selection function and then compare to predictions of population synthesis calculations carried out with a variety of MB prescriptions. Our analysis is carried out on a sample selected and spectroscopically followed-up specifically with the goal of constraining the companion mass distribution, allowing us to account and correct for selection biases when comparing models to data.

The rest of the paper is organized as follows. In Section 2, we discuss our target selection and basic properties of the sample. In Section 3, we describe our spectroscopic observations. Then in Section 4, we describe measurement of radial velocities, orbit fits, and companion mass measurements. In Section 5, we compare our observational results to the predictions of binary population synthesis models with a range of MB laws. We also discuss our results in the context of previous literature on WD + MS binaries. Finally, we conclude with a discussion of our findings and their implications in Section 6.

2. Observed Sample

2.1. Sample Selection

Although there have been several previous population studies of sdB + MS systems (e.g., Kupfer et al. 2015; Lei et al. 2020; Kruckow et al. 2021; Schaffenroth et al. 2022), these all consisted of heterogeneous population samples and were dominated by short-period binaries. Here, we construct a carefully selected sample with a well-understood selection function. We selected our targets from the list of sdB + MS

binaries published by Schaffenroth et al. (2022), who conducted an all-sky search for sdBs in close binaries using light curves from the Transiting Exoplanet Survey Satellite (TESS; Ricker et al. 2015). We focus on eclipsing systems because they are close to edge-on, meaning there is little inclination uncertainty, and we can measure the companion mass from RVs. Additionally, the detection probability of these eclipsing systems depends primarily on geometry, making it easier to model the selection function.

Schaffenroth et al. (2022) built a sample of 52 HW Vir systems by drawing from the Geier (2020) catalog of sdBs. Of these, we selected 37 systems that are brighter than $G = 16$ mag. Given the large amplitude of the reflection effect and eclipses in close sdB + MS binaries, the Schaffenroth et al. (2022) sample is essentially complete to sdB + MS binaries with $G < 16$ mag and $P_{\text{orb}} < 1$ day, if they are in the Geier (2020) catalog. Of these, we selected the 16 systems with periods between 3.8 and 12 hr. We do not include shorter period systems because those systems can only host low-mass companions ($M_{\text{MS}} \lesssim 0.3M_{\odot}$). Of these 16, one system (J0531-6953) has previously been studied in detail by Kupfer et al. (2015). Out of the remaining 15 systems, we obtained multi-epoch spectroscopic follow-up of 13 (see Table 4). Our final sample of 14 binaries is 87.5% complete with respect to the Geier (2020) sample of HW Vir systems brighter than $G = 16$ mag with periods of 3.8–12 hr. The Geier (2020) sample may not be complete in this magnitude range—it is likely to be missing some sdBs in regions of high extinction—but we show in Section 2.2.2 that the catalog's completeness is expected to be independent of companion mass over the mass range relevant to our study.

2.2. Basic Properties of the Sample

2.2.1. Orbital Ephemerides

We now investigate the 14 systems in our sample in detail. We begin by measuring orbital periods and ephemerides from their light curves.

We obtained light curves for each target from either the Zwicky Transient Facility (ZTF; Bellm et al. 2019) or the All-Sky Automated Survey for Supernovae (ASASSN; Kochanek et al. 2017). We used light curves from ZTF and ASASSN rather than TESS because they have longer time baselines (5–10 yr, compared to ~ 27 days per TESS sector), allowing for more precise period measurements. When possible, we used the ZTF r -band light curve. For targets with poor ZTF phase coverage, we used the ASASSN g -band light curves.

We calculated a Lomb–Scargle periodogram (Lomb 1976; Scargle 1982) using the Python Astropy package (Astropy Collaboration et al. 2013, 2018, 2022) to determine orbital periods. Phased and normalized light curves for each source are

shown in Figure 1, where we also indicate which survey and bandpass was used for each system. For several systems which exhibited noisy light curves after phase folding, we binned the photometric data. We binned our data into $N = 75, 100, 150$ or 300 bins, where we averaged over the fluxes within each bins. The photometric variability is dominated by quasi-sinusoidal variability on the orbital period, which is a result of irradiation of the “day” side of the MS star by the sdB. Primary and secondary eclipses are also evident for all sources, confirming their nature as HW Vir binaries. The measured periods are listed in Table 1 and their distribution is shown in Figure 2. We find that our sample has a fairly uniform period distribution with a slight excess of systems with periods of 4–5 hr.

To determine the orbital ephemerides, we fitted each light curve with a model calculated with `ellc` (Maxted 2016) for a detached eclipsing binary containing a hot sdB star and a cool MS companion. The primary goal was to determine the time of the primary eclipse, t_0 , when the MS star moves in front of the sdB. We time the first eclipse after JD 2459000, which is near the midpoint of the light curve data for most targets, in order to minimize correlations between t_0 and P_{orb} . We use the convention that phase 0 occurs at t_0 , the time of the primary eclipse.

We fixed the orbital period to the value found from the Lomb–Scargle periodogram, and model the reflection effect using the “heat” parameter (see Maxted (2016) for the details about the parameter). We report the best-fit P_{orb} and t_0 for each system in Table 1. We did not attempt to infer other physical parameters from the light curves at this stage, since our main goal is to measure the companion masses, and these are not directly constrained by the light curves.

2.2.2. Observable Parameters

We obtained other basic parameters of our targets from Gaia DR3 (Gaia Collaboration et al. 2023), including their parallax, G -band apparent magnitude, and $G_{\text{BP}} - G_{\text{RP}}$ color. These values are reported in Table 2. We obtained extinction estimates for our targets from the 3D dust maps of Green et al. (2019) and Lallement et al. (2022). We show the sources in an extinction-corrected color–magnitude diagram (CMD) in the bottom panel of Figure 2. For reference, we also show the Gaia 50 pc sample. The objects in our sample fall in the sdB clump, blueward of the MS and above the white dwarf cooling track.

The Schaffenroth et al. (2022) sample of sdB candidates from which our sample is drawn were selected on the basis of their position in the sdB clump of the CMD. Our sample is thus biased against sdB + MS binaries that do not fall in the clump. To assess the effects of this bias, we show predicted photometry of unresolved sdB + MS binaries with a range of MS star masses in the bottom left panel of Figure 2. We assume absolute magnitudes of $G, G_{\text{BP}}, G_{\text{RP}} = 4.4, 4.2, 4.6$ mag for the sdB, and we take the predicted magnitudes for the MS star from Pecaut & Mamajek (2013). We find that sdB + MS binaries are

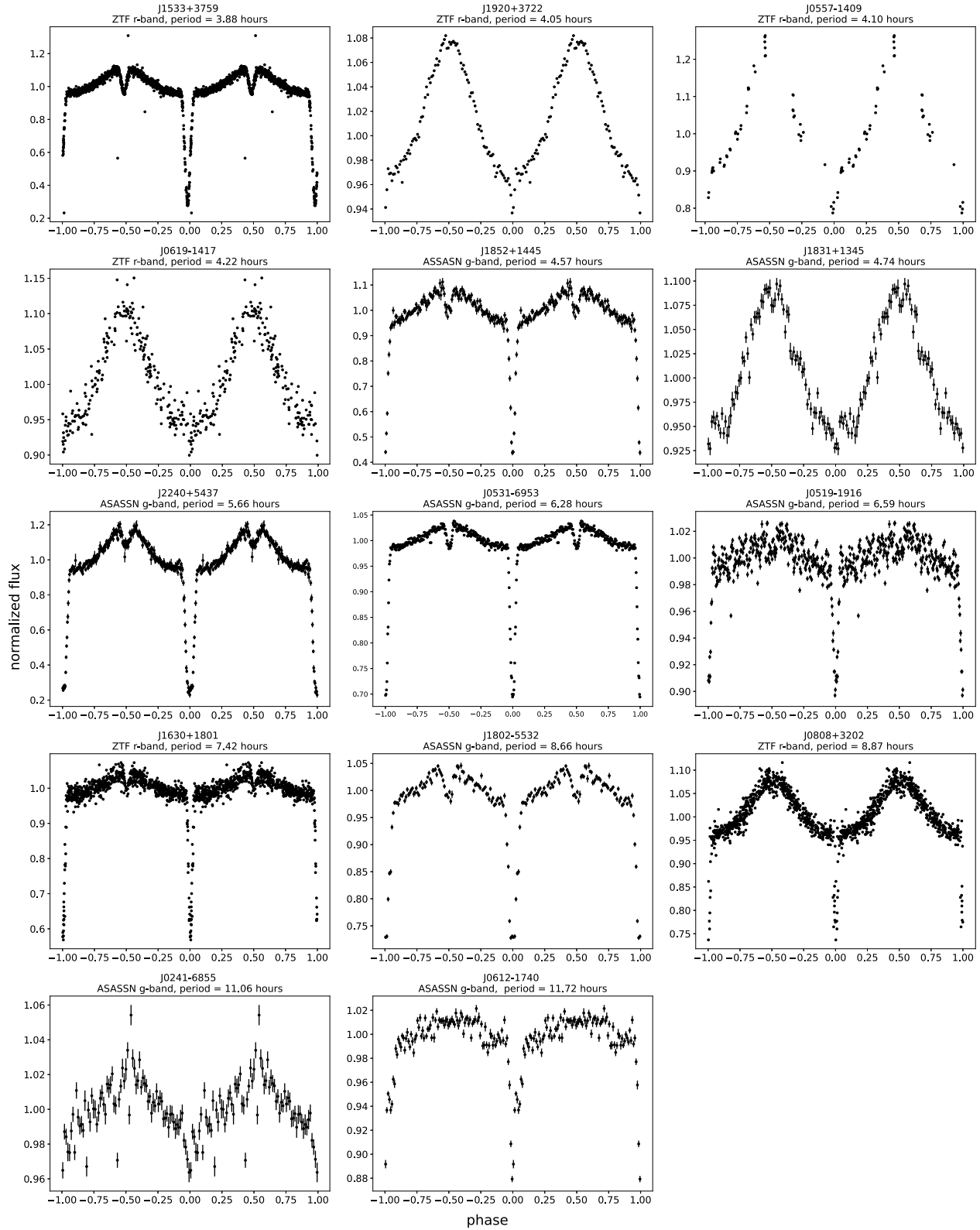


Figure 1. Phased ZTF and ASASSN light curves for all targets in our sample, organized from shortest to longest period. We define phase 0 as the time of the primary eclipse (Table 1). A secondary eclipse is also visible in most systems. Data are from ZTF and ASASSN, and the light curves are phases-folded to the periods we determined (see Table 2).

Table 1
Orbital Ephemerides for the sdB + MS Binaries in our Sample

Gaia ID	Object Name	Period (P_{orb}) (hr)	Eclipse Time (t_0) (HJD)
1375814952762454272	J1533+3759	3.882492352179863	2459000.0486605708
2051078953817324672	J1920+3722	4.054919786574039	2459000.1504712766
2995717462506292736	J0557-1409	4.096633792122831	2459000.112196558
2993468995592753920	J0619-1417	4.224256397090405	2459000.0407816754
4507223312777873280	J1852+1445	4.570024569851073	2459000.083174447
4508520908289527808	J1831+1345	4.741903317052129	2459000.2981252046
2003241230122936064	J2240+5437	5.661092569611973	2459000.0809536236
4657996005080302720	J0531-6953	6.276969603308999	2459000.14753494
2969438206889996160	J0519-1916	6.59016169200534	2459000.13163848
4467130720760209152	J1630+1801	7.4232094820660715	2459000.1136060352
6652952415078798208	J1802-5532	8.663582790263654	2459000.0554469298
901929564359845888	J0808+3202	8.873264194045575	2459000.231370364
4647004122914240640	J0241-6855	11.05915838812156	2459000.281179102
2943004023214007424	J0612-1740	11.720487447561574	2459000.4836920444

Note. The period was determined from a Lomb–Scargle periodogram, and the eclipse time was determined by fitting the light curve with a detached binary model calculated with `ellc` (see Section 2.2.1).

predicted to fall redward of the sdB clump only for MS star masses $M_{\text{MS}} \gtrsim 0.8 M_{\odot}$. This means that our sample is biased against MS companions more massive than $\sim 0.8 M_{\odot}$ (which are expected to form in wide orbits through stable mass transfer; e.g., Han et al. 2002), but not against companions with lower masses. Given their CMD position, we expect MS star masses below $0.8 M_{\odot}$ for the systems in our sample.

3. Follow-up Observations

To constrain the MS star masses, we obtained multi-epoch follow-up spectroscopy of all objects in our sample using several different instruments. We measured RVs of each target in at least three epochs obtained across at least two nights.

We used four spectrographs at three different observatories: the Low Resolution Imaging Spectrometer (LRIS; Oke et al. 1994) and Echellette Spectrograph and Imager (ESI; Sheinis et al. 2002) on the 10 m Keck I and Keck II telescopes, the Double Spectrograph (DBSP; Oke & Gunn 1982) on the 5 m Hale telescope at Palomar observatory, and the Fiber-fed Extended Range Optical Spectrograph (FEROS; Kaufer et al. 1999) on the ESO/MGP 2.2 m telescope at La Silla Observatory. We used LRIS, ESI, and DBSP for targets in the north, and FEROS for targets in the south. Below, we discuss the settings and data reduction process for each instrument.

3.1. Low Resolution Imaging Spectrometer (LRIS)

For LRIS, we observed on the blue and red arms simultaneously using a 1.0 slit. We used exposure times of 300 and 600 s (depending on the magnitude of the target), and obtained spectra covering wavelengths of $\lambda = 320\text{--}1000$ nm with a resolution of $R \sim 2000$. The data were reduced using LPipe (Perley 2019).

3.2. Echellette Spectrograph and Imager (ESI)

For ESI, we used the 0.3 slit with 2×1 binning and 300 s exposures. We obtained spectra covering $\lambda = 390\text{--}1100$ nm at a resolution of $R \sim 11,000$. We reduced the data using the MAuna Kea Echelle Extraction (MAKEE) pipeline.

3.3. Fiber-fed Extended Range Optical Spectrograph (FEROS)

From FEROS, we obtained spectra covering wavelengths $\lambda = 360\text{--}920$ nm at a resolution of $R \sim 50,000$. We used exposure times of 1800–2400 s. The data were reduced using the CERES pipeline (Brahm et al. 2017).

3.4. Double Spectrograph (DBSP)

For DBSP, we used a 1.0 or 1.5 slit (depending on seeing) and exposure times of 300–600 s (depending on the magnitude of the target). Using both the blue and red arms, we obtained spectra covering the wavelength range of $\lambda = 350\text{--}800$ nm at a resolution of $R \sim 1500$. To reduce the data, we used the `pypeit` reduction pipeline (Prochaska et al. 2020). We also applied an empirical correction for instrumental flexure to the wavelength solution using telluric absorption lines, as described by Nagarajan et al. (2023).

All our observations are listed in Table 4 in Appendix A.

4. Analysis

4.1. Radial Velocity Measurements

We normalized the spectra using a running median calculated in a 101 \AA window. We normalized the template spectra using the same method. The sdB stars dominate the

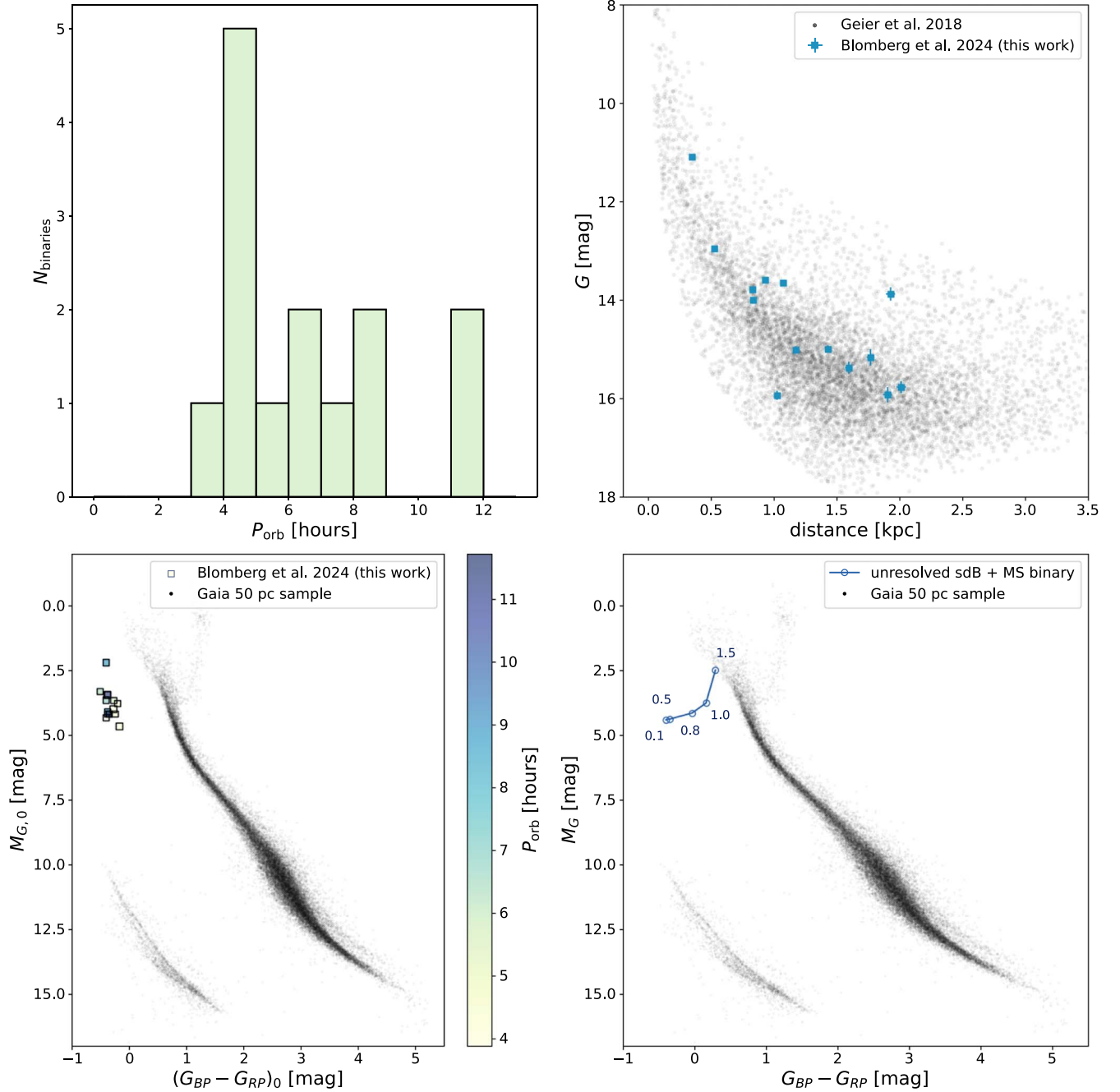


Figure 2. Top left: orbital period distribution of objects in our sample. Top right: distance (i.e., $1/\varpi$) and G -band apparent magnitude. Our sample is compared to objects in the sdB candidate catalog from Geier (2020) with $\varpi/\sigma_{\varpi} > 5$. The binaries in our sample are all within ~ 2 kpc of the Sun and have apparent magnitudes ranging from ~ 16 to 11 mag. Bottom left: objects in our sample on an extinction-corrected Gaia CMD, compared to the 50 pc sample. They all fall in the sdB clump, with little light contributions from the MS stars in the optical. Bottom right: predicted photometry for unresolved sdB + MS binaries with a range of companion masses. Hollow points shows predictions for a typical sdB paired with a MS star of mass 0.1, 0.5, 0.8, 1.0, and 1.5 M_{\odot} . Only companions with masses above 0.8 M_{\odot} are predicted to appreciably move the unresolved source away from the sdB clump.

observed spectra, and we do not detect absorption features from any of the MS companions.

We measured the RV of the sdB star in each spectrum by cross-correlating a synthetic template with the data after

applying a barycentric correction. For spectra from DBSP, ESI, and LRIS, we used templates from Nemeth et al. (2014), who calculated a grid of non-local thermodynamic equilibrium (NLTE) synthetic spectra covering $\lambda = 320\text{--}720$ nm using

Table 2
Basic Properties of sdB + MS Binaries in Our Sample

Object Name	R.A. (deg)	Decl. (deg)	G (mag)	M_G (mag)	$G_{BP} - G_{RP}$ (mag)	ϖ (mas)	$E(B - R)$ (mag)
J1533+3759	233.45601	37.99106	12.94	4.34 ± 0.04	-0.384	1.904 ± 0.035	0.02
J1920+3722	290.24905	37.37222	15.76	4.25 ± 0.12	-0.141	0.498 ± 0.029	0.11
J0557-1409	89.37149	-14.16629	15.92	5.87 ± 0.09	0.440	0.977 ± 0.040	0.47
J0619-1417	94.76123	-14.28690	15.91	4.52 ± 0.16	-0.075	0.527 ± 0.038	0.14
J1852+1445	283.03169	14.76307	14.99	4.65 ± 0.07	0.239	0.852 ± 0.025	0.34
J1831+1345	277.81563	13.75534	15.15	3.92 ± 0.17	-0.137	0.567 ± 0.045	0.19
J2240+5437	340.21327	54.63084	14.97	4.21 ± 0.07	0.011	0.701 ± 0.023	0.22
J0531-6953	82.91801	-69.88371	11.10	3.36 ± 0.03	-0.478	2.837 ± 0.044	0.03
J0519-1916	79.94864	-19.28166	13.59	3.75 ± 0.07	-0.349	1.077 ± 0.032	0.05
J1630+1801	247.68937	18.02232	15.37	4.36 ± 0.12	-0.271	0.628 ± 0.034	0.08
J1802-5532	270.70734	-55.54981	13.83	2.45 ± 0.13	-0.275	0.53 ± 0.03	0.10
J0808+3202	122.11083	32.04179	13.78	4.19 ± 0.06	-0.323	1.205 ± 0.036	0.05
J0241-6855	40.32553	-68.92373	14.64	3.50 ± 0.06	-0.354	0.933 ± 0.027	0.03
J0612-1740	93.19719	-17.67511	13.99	4.39 ± 0.05	-0.241	1.198 ± 0.026	0.09

Note. The parallax, M_G , and $G_{BP} - G_{RP}$ values are taken from Gaia DR3 (Gaia Collaboration et al. 2023); the reddening values are taken from Green et al. (2019) and Lallement et al. (2022).

Plusty and Synspec (Hubeny & Lanz 2017). Their grid provides models for a range of effective temperatures, surface gravities, and surface He abundances. Our primary goal was to measure reliable RVs. This requires a template with similar spectral lines to the observed spectra, but not necessarily one whose parameters match the true parameters of each observed sdB. Because multiple combinations of atmospheric parameters and abundances can produce similar spectra, we fixed the temperature and surface gravity to typical values for sdBs: $T_{\text{eff}} = 35,000$ K and $\log(g/[\text{cm s}^{-2}]) = 5.0$, and chose the model for each observed sdB with He abundance that best matched the observed spectra. We then used the same template for all observations of a given system.

We cross-correlated the template and observed spectra over wavelengths $\lambda = 640\text{--}680$ nm, which contain the $\text{H}\alpha$ absorption line ($\lambda = 656.46$ nm) and a strong He I absorption line ($\lambda = 667.82$ nm). For spectra taken with FEROS, which have higher resolution and therefore contain several resolved narrow metal lines, we instead used the wavelength range of $\lambda = 450\text{--}550$ nm, which contains several narrow metal lines. Since these metal lines are not present in the Nemeth et al. (2014) models, we instead used a bespoke template generated with Plusty and Synspec (Hubeny & Lanz 2017), assuming solar metallicity. We convolved each of the spectral templates with a Gaussian kernel of appropriate FWHM to account for instrumental broadening for each instrument. The formal RV uncertainties are small ($\lesssim 1$ km s $^{-1}$). However, we expect the true uncertainties to be dominated by systematics, such as flexure and zerpoint offsets between different instruments. Therefore, we adopted conservative uncertainties of 10 km s $^{-1}$ for DBSP and LRIS, and 5 km s $^{-1}$ for ESI and FEROS, based on the RV stability of standard stars observed with the same

setup. The RV measurements for all of the spectra are listed in Table 4 in Appendix A. Some of our fits, representative of our observed population, are shown in Figure 3 for reference.

4.2. RV Curves

Using the ephemerides obtained from the light curves, we fit the observed RVs to constrain the RV semi-amplitudes of the sdB stars and the binaries' center-of-mass velocities. For each target, we fitted the measured RVs with a sinusoid:

$$\text{RV} = -K \sin\left(\frac{2\pi(t - t_0)}{P_{\text{orb}}}\right) + \gamma, \quad (1)$$

where K is the semi-amplitude of the velocity variation of the sdB, t_0 is the time of the primary eclipse (Table 1), P_{orb} is the orbital period, and γ is the center of mass velocity. Equation (1) assumes a circular orbit, which is expected for our systems since the periods are short enough to be circularized by tides. We fit the data using `emcee` (Foreman-Mackey et al. 2013) to sample from the posterior, adopting broad flat priors on the free parameters K and γ . The results of the fit are shown in Figure 4, and the inferred parameters are listed in Table 3. For J0531-6953, we show the best-fit RV curve measured by Kupfer et al. (2015).

4.3. Companion Masses

Our constraints on the sdB stars' RV semi-amplitudes allow us to constrain the companion masses, subject to assumptions about the inclination and the sdB mass. We first compute the RV mass function,

$$f_m = \frac{P_{\text{orb}} K^3}{2\pi G}. \quad (2)$$

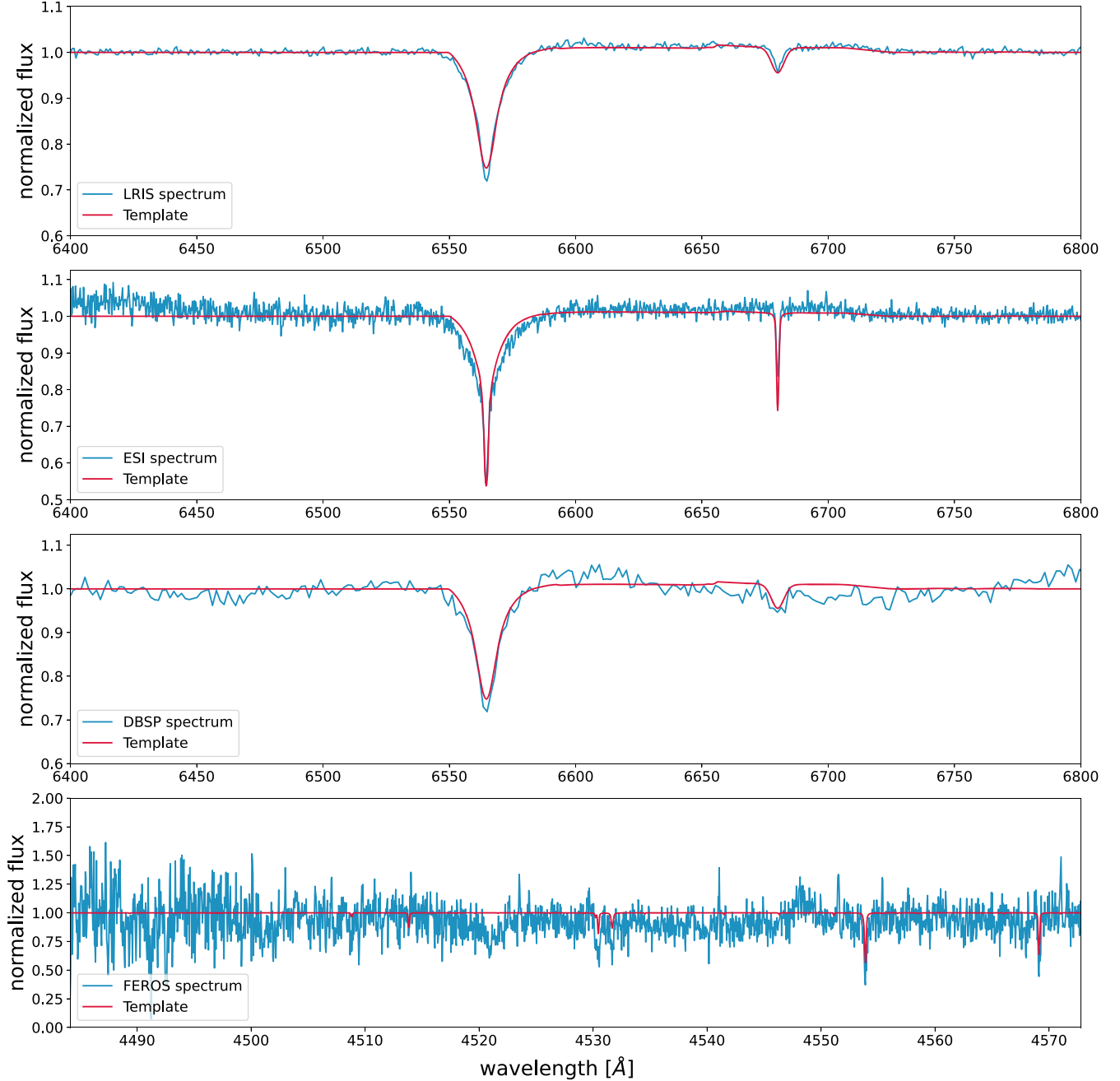


Figure 3. Example spectra from LRIS, ESI, DBSP, and FEROS. We overplot a model spectrum with the inferred RV in each panel. The top three panels show spectra of J0519-1916, and the best-fit synthetic spectrum from Nemeth et al. (2014). The $H\alpha$ and He I lines provide the primary RV constraint. The bottom plot shows a FEROS spectrum for J1802-5532 and corresponding model spectrum; here the RV constraint comes from narrow metal lines.

The mass function is related to the component masses and orbital inclination:

$$f_m = \frac{M_{\text{MS}}^2 \sin^3 i}{(M_{\text{sdB}} + M_{\text{MS}})^2}. \quad (3)$$

P_{orb} and K are constrained by the light curves and RV measurements, respectively. Further, since we limited our study

to eclipsing systems, we expect the inclinations to be close to 90° . For a given choice of sdB mass and inclination, we can then numerically solve Equation (3) for the mass of the MS companion. Figure 5 illustrates how our constraints on P_{orb} and K then translate to constraints on M_{MS} . Higher assumed sdB masses and lower assumed inclinations translate to higher MS star masses, but the dependence on both of these quantities are weak within their plausible ranges for eclipsing systems.

To determine the uncertainties on the companion mass, we produced a distribution of masses using a Monte Carlo simulation. For each target, we randomly sampled 50 RV semi-amplitudes from the MCMC posterior distribution produced when fitting the RV curves. Further, we sampled 100 sdB masses from a uniform distribution, $\mathcal{U}(0.45, 0.55) M_{\odot}$ (Han et al. 2003). Then for each sdB mass in our sample, we sampled 100 inclination angles from a $\sin(i)$ inclination distribution between i_{\min} and 90° , where i_{\min} is the minimum possible inclination angle for a system with a given period to eclipse. From the geometry of the system, we can solve for the minimum inclination angle, i_{\min} , using the relation:

$$\cos(i_{\min}) = \frac{R_{\text{MS}} + R_{\text{sdB}}}{a}. \quad (4)$$

Using Kepler's laws, we can rewrite this as:

$$\cos(i_{\min}) = (R_{\text{MS}} + R_{\text{sdB}}) \left(\frac{4\pi^2}{GP_{\text{orb}}(M_{\text{MS}} + M_{\text{sdB}})} \right)^{1/3}. \quad (5)$$

We took a typical sdB mass ($M_{\text{sdB}} = 0.5M_{\odot}$) and a radius $R_{\text{sdB}} = 0.21R_{\odot}$, corresponding to a surface gravity $\log(g[\text{cm s}^{-2}]) = 5.5$. For the MS star, we took a mass $M_{\text{MS}} = 0.3M_{\odot}$ and radius $R_{\text{MS}} = 0.29R_{\odot}$, as predicted by MIST isochrones (Choi et al. 2016). This value is conservative, since we will show that most MS stars in the sample have masses lower than $0.3 M_{\odot}$, and i_{\min} corresponds to very shallow grazing eclipses. For each system, we calculated i_{\min} by solving Equation (5) using P_{orb} determined from the light curves. For each K , we numerically solved Equation (3) for each combination of the sampled sdB mass, inclination, and mass function. This procedure produces an approximately Gaussian distribution of dynamically implied MS star masses (right panel of Figure 5). We report the median and standard deviation of this distribution as the best-fit MS star mass and corresponding uncertainty in Table 3.

Our assumption of $M_{\text{sdB}} \sim \mathcal{U}(0.45, 0.55) M_{\odot}$ is reasonable for the canonical sdB formation channel, but some sdBs can have higher or lower masses (e.g., Han et al. 2002), and we cannot rule out this possibility for any given system. To assess the impacts of the assumed sdB mass on our results, we explore more extreme masses of $M_{\text{sdB}} = 0.35M_{\odot}$ and $M_{\text{sdB}} = 0.60M_{\odot}$ in Appendix B. We find that our results are only weakly sensitive to the assumed sdB mass even over this rather broad range.

4.4. Population Properties

Figure 6 shows the inferred companion masses and orbital periods of binaries in our sample. We compare to other HW Vir binaries with companion mass constraints from the literature compilation by Schaffenroth et al. (2018).

The companion mass distribution for both samples of HW Vir binaries peaks at $0.1\text{--}0.15M_{\odot}$ and falls off above $0.2 M_{\odot}$.

This is reminiscent of the lack of higher-mass MS stars in WD + MS binary samples that has been interpreted as evidence for DMB (e.g., Schreiber et al. 2010). Unlike the previous literature, our sample does contain two binaries with companion masses near $0.4 M_{\odot}$, above the fully convective limit. However, the bulk of the population has lower M_{MS} .

The right panel of Figure 6 shows the companion masses and orbital periods of sdB + MS binaries from both samples. The black line marks the Roche lobe overflow limit. Compared to the previous literature, our sample includes a wider range of orbital periods and companion masses. Crucially, we focused on long orbital periods ($P_{\text{orb}} > 3.8$ hr) because these orbits are wide enough to accommodate a wide range of MS star masses. In contrast, most of the previously studied systems have orbital periods of 1–3 hr, which can only accommodate low-mass companions ($M_{\text{MS}} \lesssim 0.3 M_{\odot}$), since higher-mass MS stars would overflow their Roche lobes (black line). Below the fully convective limit, the mass distribution of our sample is similar to that found at shorter periods in the literature. There is no significant correlation between companion mass and orbital period in our sample.

4.5. Selection Effects and Biases

Our sample was selected to (a) be brighter than $G = 16$ mag, (b) have $P_{\text{orb}} = 3.8\text{--}12$ hr, and (c) be eclipsing. We can model the effects of each cut.

Given that typical sdBs have $M_{G,0} \approx 4$ (Heber 2016) (a) translates to a distance limit of ≈ 2.5 kpc, or closer for systems with significant foreground extinction. We do not expect $M_{G,0}$ to be significantly correlated with companion mass, since the MS companions contribute $\lesssim 1\%$ of the optical light for $M_{\text{MS}} \lesssim 0.5 M_{\odot}$.

The cut on orbital period, (b), corresponds to a range of allowed companion masses, since only low-mass MS stars are sufficiently dense to fit in the shortest-period orbits without overflowing their Roche lobes (Figure 7). However, this does not lead to a significant bias in our sample, because MS stars with masses $\lesssim 0.5M_{\odot}$ could fit inside the full range of orbital periods represented in our sample.

Finally, the requirement that binaries be eclipsing leads to a quantifiable bias against low-mass MS companions. Appendix C shows how the eclipse probability varies with MS companion mass and orbital period. The mass of the sdB star has little effect on the eclipse probability, with less than 5% variations in the eclipse probability for $M_{\text{sdB}} = 0.3\text{--}0.6M_{\odot}$ assuming $\log(g/[\text{cm s}^{-2}]) = 5.5$ when the mass of the companion and the period are held constant. Figure 7 shows the predicted eclipse probability as a function of orbital period and MS star mass, assuming a fixed sdB star mass of $0.5 M_{\odot}$.

At a fixed period, the predicted eclipse probability rises monotonically with M_{MS} , since higher-mass MS stars have larger radii. Our targets span a wide range of periods but all

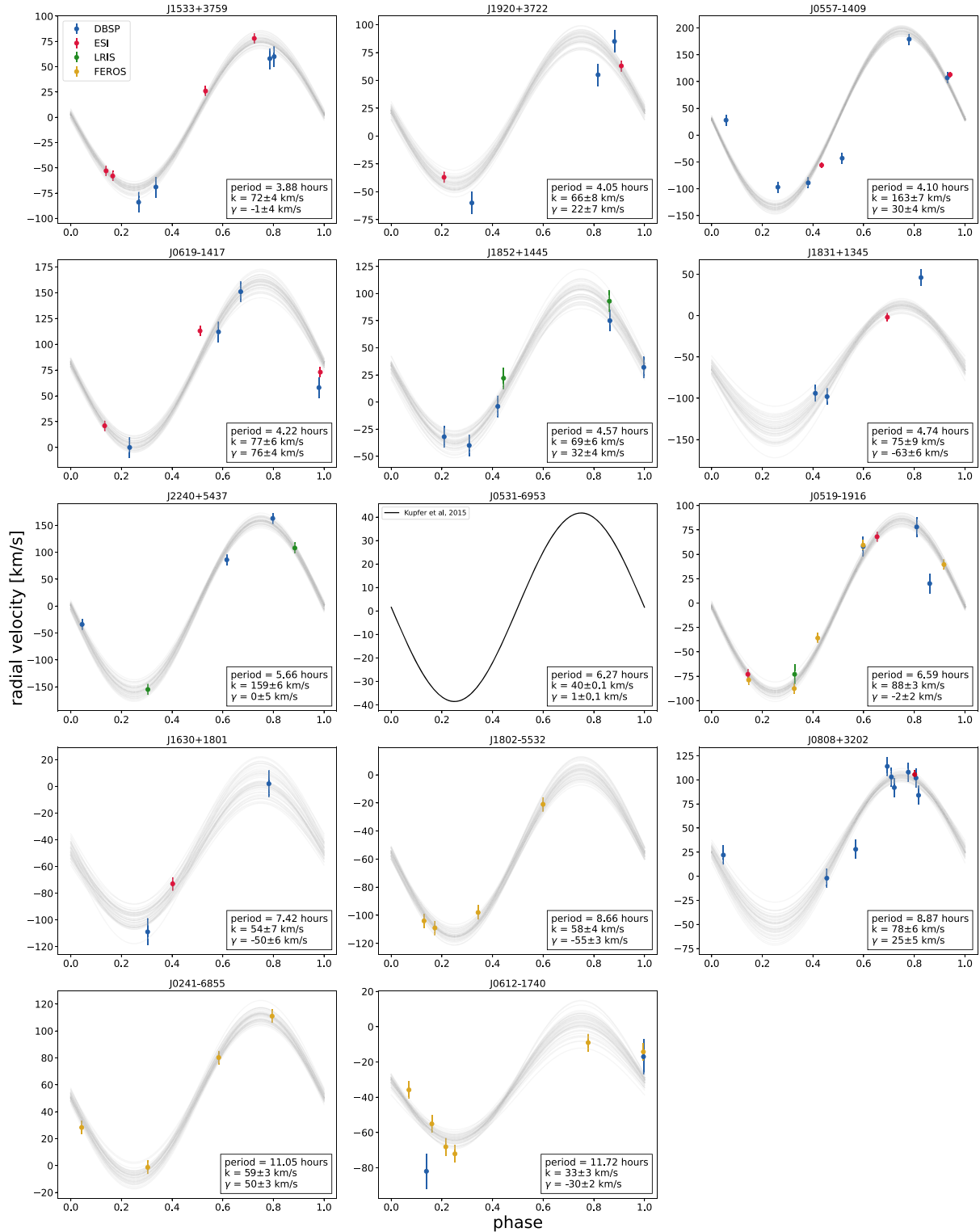


Figure 4. Measured RVs as a function of orbital phase for each target. The colors of data points correspond to which instrument the measurement was made with. We fit the observed RVs with a sinusoidal model (Equation (1)), fixing the orbital period and eclipse time to the value measured from the light curve. This allows us to constrain the RV curves robustly even with only a few data points. Gray lines show random samples from the posterior. The corresponding constraints are listed in Table 3. The RV curve for J0531-6953 is taken from a previous study by Kupfer et al. (2015).

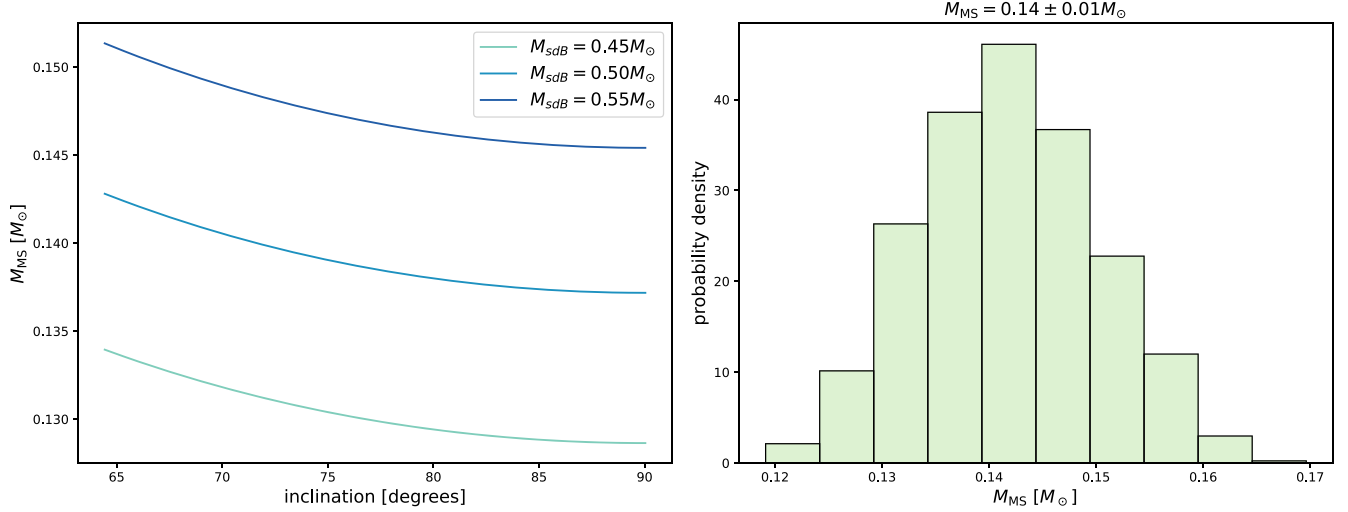


Figure 5. Companion mass constraints for J1533+3759, a typical object in our sample. Left: companion mass implied by the sdB RV mass function (Equation (3)) for various sdB masses $M_{\text{sdb}} = (0.45\text{--}0.55)M_{\odot}$ and inclination angles $i = 64.4^{\circ}\text{--}90.0^{\circ}$. Right: the companion mass distribution produced from 100 samples of sdB mass from $\mathcal{U}(0.45, 0.55) M_{\odot}$, 100 samples of inclination from a $\sin(i)$ inclination distribution for eclipsing systems ranging from 64.43° to 90.0° , and 50 samples of the RV semi-amplitude K from the posterior of the MCMC fitting. The median and standard deviation of the inferred M_{MS} values are reported as the best-fit companion mass and its uncertainty.

have relatively low companion masses and thus fall in the regime of 20%–30% eclipse probabilities. The lack of higher-mass MS stars in our sample cannot be a selection effect driven by our requirement that binaries be eclipsing, since eclipse probabilities favor high-mass companions. More massive MS companions also lead to higher-amplitude reflection effects that are more easily detectable. This means that the intrinsic drop-off in the companion mass distribution must be even stronger than what is found in our observed sample.

4.6. Comparison to Other PCEB Populations

Figure 8 compares our observed sample to populations of sdB + WD (left panel) and WD + MS (right panel) binaries from Schaffenroth et al. (2022) and Zorotovic et al. (2010), respectively.

The WD + sdB binary population represents a population of PCEBs that presumably have not undergone MB, since neither component of the binary is expected to experience MB. At $P_{\text{orb}} > 3.8$ hr, the effects of gravitational wave angular momentum losses are also expected to be negligible during the ~ 100 Myr lifetime of the sdB stars. Thus, we expect this population to be representative of the zero-age PCEBs that have not yet undergone any period evolution due to MB. Here, the measured WD masses from Schaffenroth et al. (2022) are lower limits, since the inclinations are unknown, and we expect the true masses to be larger. This suggests that WD companions to sdB stars have significantly higher masses at shorter periods than do MS companions,

Table 3
sdB RV Semi-amplitudes and Center-of-mass RVs Measured from Our Follow Up

Object Name	K (km s^{-1})	γ (km s^{-1})	M_{MS} (M_{\odot})
J1533+3759	72.39 ± 4.14	-1.87 ± 3.53	0.14 ± 0.01
J1920+3722	66.14 ± 3.80	22.78 ± 3.05	0.12 ± 0.01
J0557-1409	163.88 ± 5.09	30.54 ± 2.70	0.41 ± 0.02
J0619-1417	77.15 ± 6.16	76.28 ± 3.79	0.16 ± 0.01
J1852+1445	69.33 ± 5.64	32.69 ± 3.89	0.14 ± 0.01
J1831+1345	75.54 ± 6.25	-63.30 ± 5.08	0.16 ± 0.02
J2240+5437	159.65 ± 6.27	-0.41 ± 4.66	0.46 ± 0.03
J0531-6953 ^a	40.15 ± 0.11	1.59 ± 0.08	0.09 ± 0.01
J0519-1916	88.84 ± 2.83	-2.85 ± 1.98	0.22 ± 0.01
J1630+1801	54.95 ± 6.89	-50.09 ± 5.92	0.12 ± 0.02
J1802-5532	58.62 ± 4.10	-55.74 ± 3.12	0.15 ± 0.02
J0808+3202	78.82 ± 6.16	-25.77 ± 5.23	0.21 ± 0.02
J0241-6855	59.82 ± 3.45	50.70 ± 2.52	0.17 ± 0.01
J0612-1740	33.54 ± 2.85	-30.49 ± 2.23	0.09 ± 0.01

Notes. We calculate the companion mass and its uncertainty from Monte Carlo samples of the semi-amplitude, orbital period, inclination, and sdB mass (see Figure 5).

^a Parameters for J0531-6953 were taken from Kupfer et al. (2015) and propagated to constraints on M_{MS} using the same procedure as for the objects we followed-up.

similar to what Kupfer et al. (2015) found in their analysis of sdB binaries.

The WD + MS binary population represents a population of binaries that have presumably evolved under the same MB law as our sdB + MS sample. Given the longer observable lifetime of WDs, we expect this population to

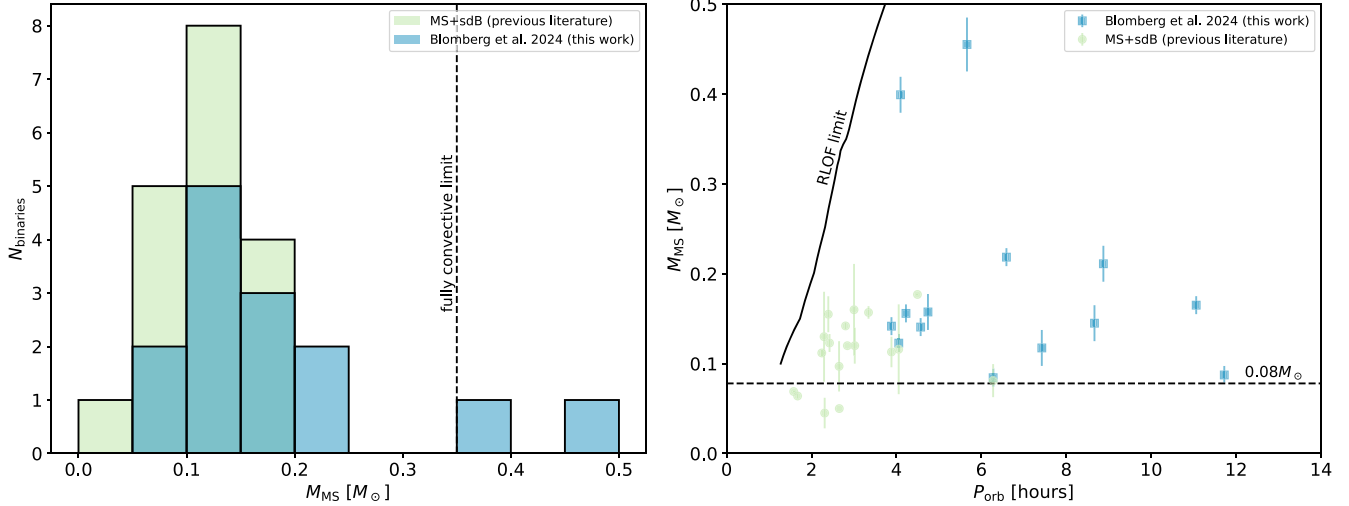


Figure 6. Left panel: mass distribution of the MS companions to sdB stars. We compare our sample (blue) to a literature compilation by Schaffenroth et al. (2018, green). Dashed lined marks the fully convective limit. The mass distribution is peaked near $0.15M_{\odot}$ in both samples, with a drop-off above $0.2M_{\odot}$ (somewhat lower than the fully convective limit), though our sample also contains two systems with $M_{MS} \sim 0.4M_{\odot}$. Right panel: companion mass vs. orbital period. Dashed line marks the hydrogen burning limit and the solid line marks the Roche lobe overflow limit. Compared to the previous literature, our sample probes longer orbital periods, which could have accommodated more massive MS companions than the short-period systems studied in previous work. However, most of the objects in our sample have low MS star masses, similar to previous literature samples.

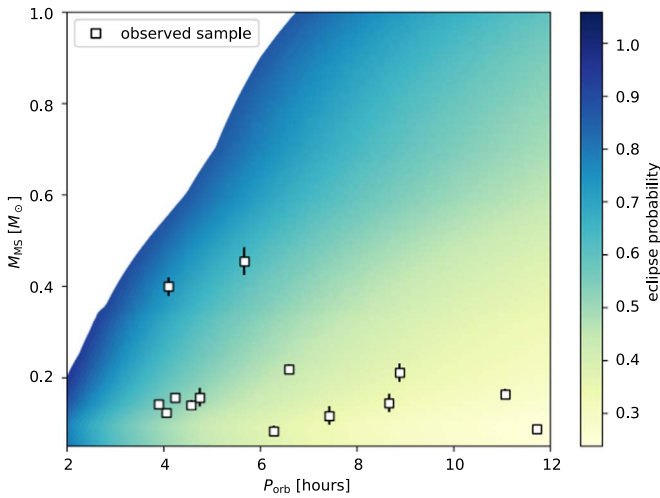


Figure 7. Eclipse probability for sdB + MS binaries, assuming randomly oriented orbits, $M_{\text{sdb}} = 0.5 M_{\odot}$, and $\log(g[\text{cm s}^{-2}]) = 5.5$. The white region in the upper left corresponds to binaries in which the MS star would overflow its Roche lobe. Our targets are shown with white squares. They have periods ranging from 3.8 to 12 hr—long enough to accommodate MS star mass up to $0.45 M_{\odot}$ at all periods, and up to $0.7 M_{\odot}$ for $P_{\text{orb}} \gtrsim 6$ hr. At fixed P_{orb} , the eclipse probability is higher for higher-mass MS stars, which have larger radii. Our selection of eclipsing systems thus leads to a bias against high-mass companions. Nevertheless, low-mass companions dominate the observed sample, suggesting that they dominate the full population.

represent older binaries compared to our observed sample, and thus to have experienced more MB-driven orbital inspiral. Compared to our sdB + MS population, we find that the WD + MS population is uniformly distributed across

a larger companion mass range ($\sim 0.1\text{--}0.4M_{\odot}$) and drops off at a higher companion mass near $M_{MS} \sim 0.4M_{\odot}$. We note that selection biases for WD + MS binaries favor low-mass companions, since higher-mass companions outshine WDs. The excess of higher-mass MS companions to WDs relative to sdBs is thus unlikely to be driven by selection effects. This suggests that if the drop-off in the companion mass distribution toward higher masses is a result of DMB, then it operates even more strongly in sdB + MS binaries than in WD + MS binaries. We explore constraints on MB further below.

5. Comparison to Simulations

To interpret the observed population and constrain formation models, we produced a synthetic population of close sdB + MS binaries using the Compact Object Synthesis and Monte Carlo Investigation Code (COSMIC; Breivik et al. 2020) and evolved the simulated binaries under various MB prescriptions. We applied the selection function of our observed sample to the simulated population and then compared this simulated and mock-observed population to our observed sample. We tested two MB prescriptions: the RVJ MB model (Verbunt & Zwaan 1981; Rappaport et al. 1983), and the saturated MB model (Kawaler 1988; Chaboyer et al. 1995; Sills et al. 2000). We also experimented with re-scaling the strength of MB above and below the fully convective boundary, following Belloni et al. (2024).

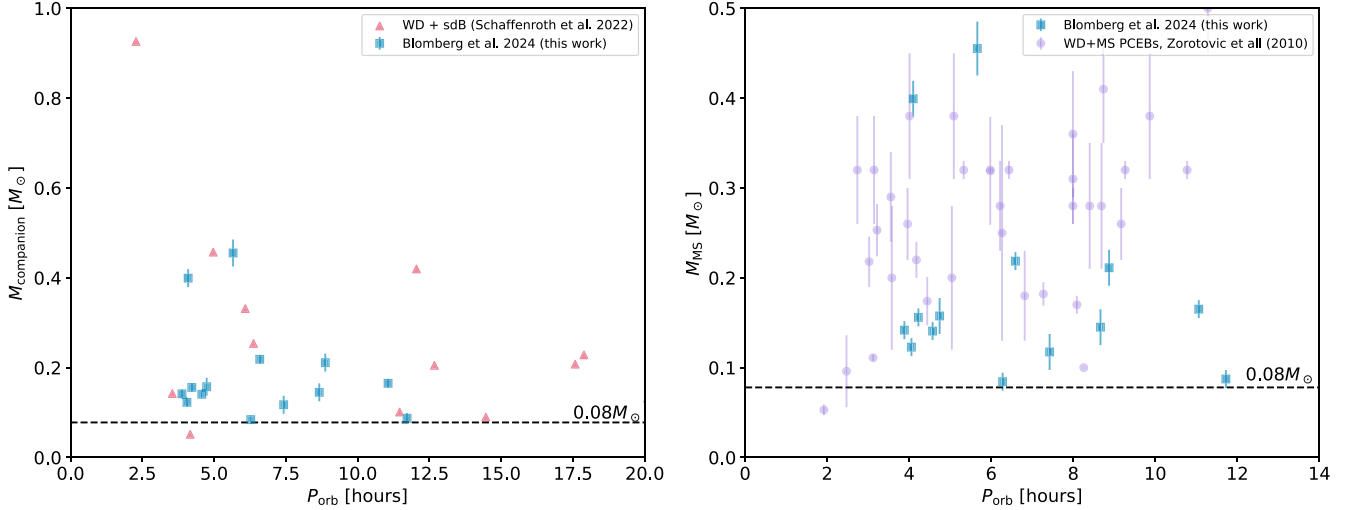


Figure 8. Left panel: observed sample compared to a population of sdB + WD systems from Schaffneroth et al. (2022). Dashed line marks the hydrogen burning limit. The WD masses from Schaffneroth et al. (2022) are lower limits and we expect the true masses to be larger, near the typical WD mass of $\sim 0.5\text{--}0.6M_{\odot}$. Right panel: observed sample compared to a population of WD + MS systems from Zorotovic et al. (2010). The WD + MS systems are distributed across a larger companion mass range ($\sim 0.1\text{--}0.4M_{\odot}$), compared to the sdB + MS systems which tend to have lower companion masses.

5.1. Producing an Initial PCEB Population with COSMIC

We used COSMIC to produce a population of zero-age PCEBs representative of the sdB + MS binaries in our sample. We assumed a Kroupa (2001) primary initial mass function, a uniform initial eccentricity distribution, and a lognormal initial period distribution following Raghavan et al. (2010). We simulate a single burst of star formation and evolve the resulting binary population for 13.7 Gyr. Since BSE (Hurley et al. 2002) and COSMIC do not model the formation of sdB stars via the standard channels (e.g., Han et al. 2002, 2003), these calculations do not directly form sdBs. Instead, when a primary overflows its Roche lobe near the tip of the first giant branch, it simply forms a He WD. Thus, we focus our analysis on PCEBs containing $0.4\text{--}0.5M_{\odot}$ He WDs, many of which should have ignited core He burning near the tip of the first giant branch and formed sdB stars. We selected binaries that any point in their evolution contain $0.4\text{--}0.5M_{\odot}$ He WDs ($kstar_1 = 10$) and MS companions with masses $M_{MS} < 0.7M_{\odot}$ ($kstar_2 = 0$). We explore the effects of selecting lower-mass sdBs, as might be expected for sdBs formed from progenitors that ignited helium non-degenerately, in Appendix E.1. While this selection is not identical to the sdB binaries in our observed sample, the stellar properties at the onset of and emergence from the common envelope are sufficiently described to capture the companion mass and orbital period distribution of the sdB sample, even though the models do not capture the ignition of He in the core. We take this population produced by COSMIC to be the zero-age sdB + MS PCEB population.

Figure 9 compares the synthetic population of sdB + MS binaries produced with COSMIC with our observed sample.

The zero-age PCEBs from COSMIC have a fairly uniform companion mass distribution, with only a gradual drop-off toward higher M_{MS} , and significantly more high-mass companions than the observed sample. This suggests that MB may play an important role in the period evolution of sdB + MS systems. In the following sections, we will evolve the synthetic population under various MB laws and compare those results to our observed population.

5.2. Evolution Under Magnetic Braking

We analytically evolved the orbital periods of the PCEBs produced by COSMIC under two MB laws following El-Badry et al. (2022). Since El-Badry et al. (2022) modeled the evolution of MS + MS binaries in which both components contribute to the angular momentum loss, we modify their formalism to only include angular momentum losses due to the MS star. Following El-Badry et al. (2022), we assume that the binary is tidally locked, meaning that the MS star's rotation period is equal to the orbital period, which is consistent with the COSMIC models which assumes tidal synchronization for all Roche lobe overflow binaries.⁵ Due to the tidal locking, the angular momentum losses from MB ultimately shrink the orbits. We neglect rotational angular momentum and changes in the component masses and

⁵ In fact, at the longer periods represented in our sample, the sdB is unlikely to be fully synchronized (Preece et al. 2018; Ma & Fuller 2024), but the MS companion is, which is sufficient for MB to operate. When the sdB becomes synchronized at $P_{orb} \approx 6\text{--}8$ hr, orbital inspiral will temporarily accelerate as orbital angular momentum is used to spin up the sdB (e.g., Schaffneroth et al. 2021). For a typical system in our sample with $M_{sdB} = 0.5M_{\odot}$, $M_{MS} = 0.3M_{\odot}$, and $P_{orb} = 8$ hr, we find that the orbital angular momentum exceeds the spin angular momentum of the sdB by a factor of ~ 1000 . We therefore do not attempt to model the effects of synchronization.

radii during the sdB + MS phase, as well as gravitational wave angular momentum losses. We evolve each binary for a time randomly drawn from $\mathcal{U}(0, 200)$ Myr, which is appropriate for a typical sdB lifetime of ~ 200 Myr (Heber 2016) and a constant star formation rate. Lower-mass sdBs have longer helium-burning lifetimes of up to 500 Myr. We show results of the same analysis with an evolution time of $\mathcal{U}(0, 500)$ Myr in Appendix E.2. Finally, we draw a random sub sample of the simulated population according to the binaries' eclipse probability (see Appendix C). Below, we outline the analysis for the RVJ and the saturated MB prescriptions evolved for $\mathcal{U}(0, 200)$ Myr.

5.2.1. RVJ Magnetic Braking Model

In the RVJ model, the MB torque is given by:

$$j_{\text{RVJ}} = -a_{\text{RVJ}} \left(\frac{M}{M_{\odot}} \right) \left(\frac{R}{R_{\odot}} \right)^4 \left(\frac{P_{\text{rot}}}{1\text{d}} \right)^{-3} \quad (6)$$

where $a_{\text{RVJ}} \approx 6.8 \times 10^{34}$ erg. Following Belloni et al. (2024), we introduce two parameters k and η that control the strength of MB above and below the fully convective boundary:

$$j = \begin{cases} k j_{\text{RVJ}}, & M_{\text{MS}} > 0.35 M_{\odot} \\ \frac{k}{\eta} j_{\text{RVJ}}, & M_{\text{MS}} < 0.35 M_{\odot} \end{cases} \quad (7)$$

We describe the analytic period evolution with these modifications in D.1.

Figure 10 compares our observed sdB + MS sample to the results of our simulations for populations evolved under the RVJ MB prescription (Equation (D1)) for a range of k and η . In each panel, the colored, circular points represent the simulated sdB + MS population evolved under the RVJ MB prescription with the specified k and η . The zero-age PCEB population was created using COSMIC as described in Section 5.1, then evolved and mock-observed using the methods described in Appendix C. The histograms show the period and companion mass distributions of the simulated and observed populations, normalized to the same scale.

The top left panel of Figure 10 shows the results for an RVJ-like MB prescription with no disruption ($k = 1, \eta = 1$). The simulated population has a fairly uniform companion mass distribution, with a weaker drop-off toward higher companion masses than found in the observed population. We expect the drop in the number of systems above the fully convective limit to be caused by the disruption in MB; thus, this suggests that our observed population could be reproduced better with a MB prescription with disruption. The top right panel shows the results for a disrupted RVJ prescription ($k = 1, \eta = 20$). Although the simulated companion mass distribution peaks below the fully convective limit, there are more predicted companions with $M_{\text{MS}} > 0.35 M_{\odot}$ than we find in the observed

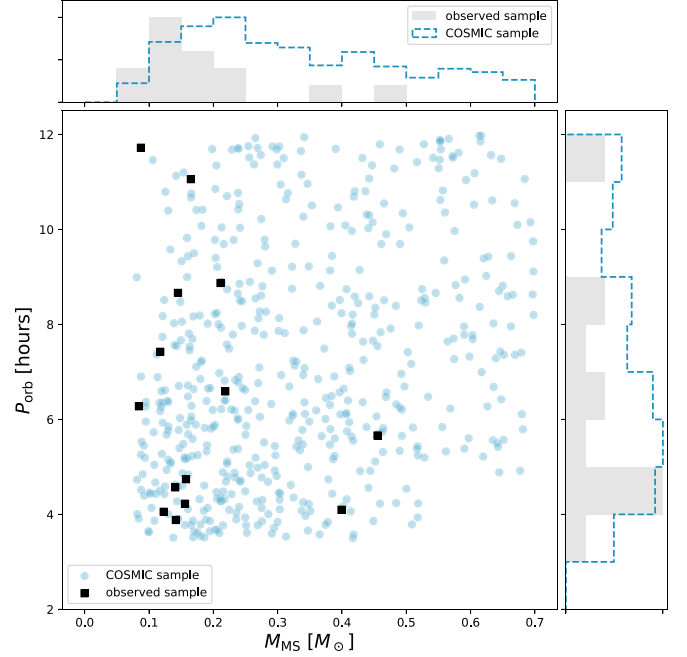


Figure 9. Comparison of the synthetic zero-age PCEB sdB + MS population produced using COSMIC with our observed sample. The zero-age PCEB population has a broad range of MS companion masses, unlike the observed population, which is dominated by companions with $M_{\text{MS}} < 0.2 M_{\odot}$.

population. This suggests that if we assume MB is the only process that is removing angular momentum from our systems, the default RVJ prescription (i.e., $k = 1$) is not strong enough to produce a sharp decrease in the number of system above the fully convective limit. The bottom left panel shows the results for boosted MB without disruption ($k = 20, \eta = 1$). This model again produces a fairly uniform companion mass distribution which suggests that boosting alone does not predict the observed population well. The bottom right panel shows the results for boosted MB with disruption ($k = 20, \eta = 20$). The simulated population best predicts the observed population for this model.

To assess whether the observed and simulated populations are consistent with one another, we apply a two-sample Kolmogorov–Smirnov (KS) test to their companion mass distributions. We find a p -value of $\sim 1\%$ for the boosted and disrupted model with ($k \gtrsim 20$ and $\eta \gtrsim 20$) whereas for the other three models, we find p -values of $0.01\%–0.05\%$. These values suggests that the observed population is not formally consistent with any of the simulated populations, reflecting the fact that the observed distribution drops off at $M_{\text{MS}} \gtrsim 0.2 M_{\odot}$ instead of $\gtrsim 0.35 M_{\odot}$. However, the boosted and disrupted RVJ model with $k \gtrsim 20$ and $\eta \gtrsim 20$ best matches the data. The small size of the observed population and imperfect match with simulations prevent us from placing precise constraints on k and η .

In summary, we find that boosted and disrupted MB model best predict the observed population for the RVJ MB prescription. Here we remain agnostic about the possible

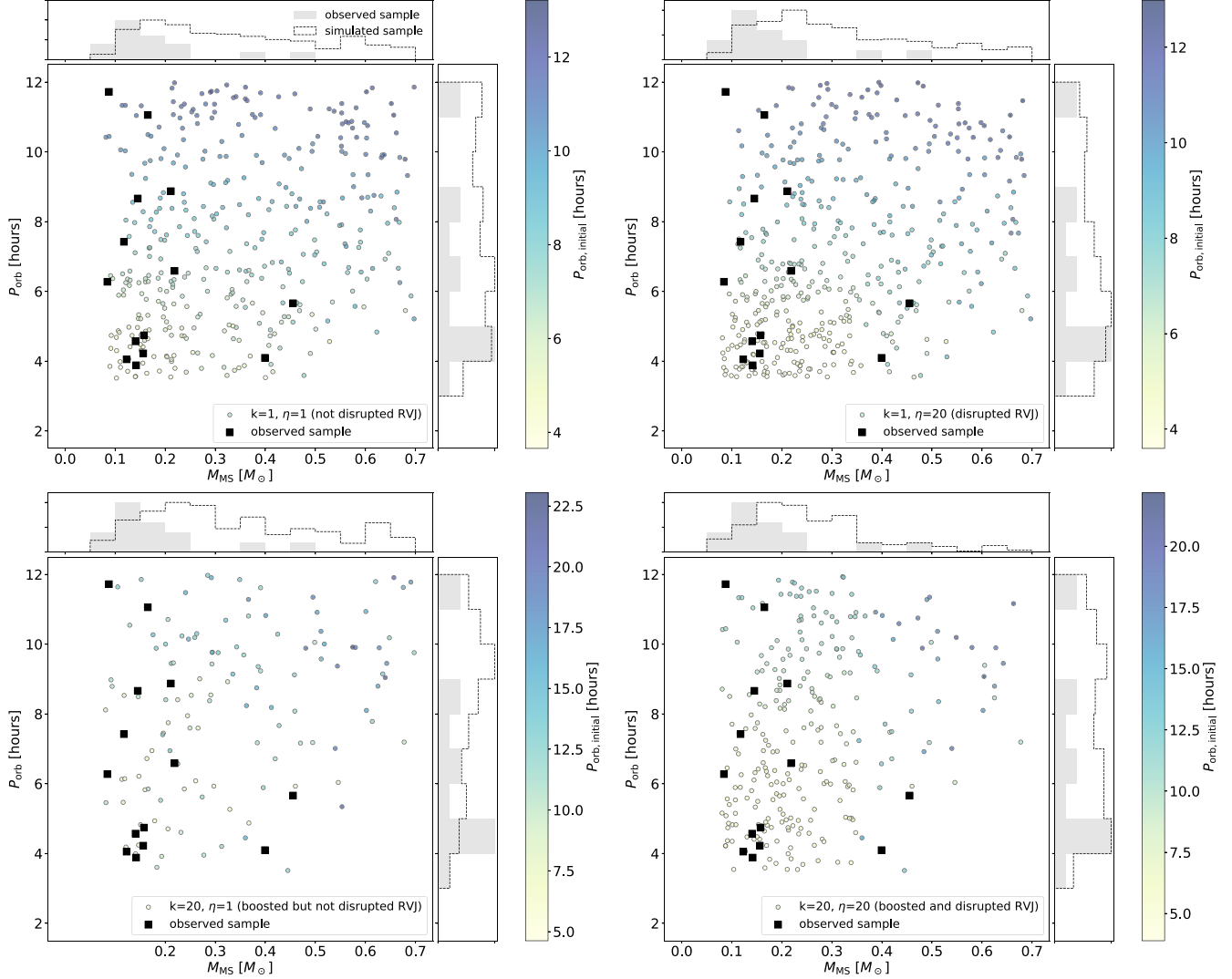


Figure 10. Simulations of a population of sdB + MS binaries evolved under the *RVJ* MB prescription (Equation (6)). Black points show our observed sample. Colored points show the result of producing a zero-age PCEB population with COSMIC, evolving their orbital periods for $\mathcal{L}(0, 200)$ Myr according to Equation (D1), and finally selecting eclipsing systems assuming randomly oriented orbits. All histograms are normalized by their tallest bin. Although this is not representative of the actual bin heights, it allows for a better comparison between the observed and simulated distributions. Each of the panels show the simulated results for various rescalings k and η (see Equation (7)). The boosted and disrupted model ($k = 20, \eta = 20$) matches the observed population best. The fiducial *RVJ* model predicts little period evolution within 100 Myr, and thus too many companions with $M_{\text{MS}} > 0.35M_{\odot}$.

physical origins of this stronger MB. We discuss possibilities and the physical plausibility of boosting MB in sdB + MS binaries further in Section 6.

The period distribution of the simulated population is fairly uniform for all simulations. This can be explained by the large number of surviving systems having a low-mass companion and therefore not experiencing strong MB.

5.2.2. Saturated Magnetic Braking Model

We next consider a saturated MB law, which predicts a MB torque whose strength scales more weakly with orbital period than the *RVJ* law (e.g., Kawaler 1988; Chaboyer et al. 1995).

We explore the saturated MB prescription because El-Badry et al. (2022) found that the *RVJ* MB model predicts a too-steep scaling with P_{orb} at short periods to match the observed MS + MS binary population. Our modeling of the saturated MB law follows El-Badry et al. (2022). The MB torque is given by:

$$j_{\text{sat}} = \begin{cases} -a_{\text{sat}} \left(\frac{P}{1 \text{ d}} \right)^{-3} \left(\frac{R}{R_{\odot}} \right)^{1/2} \left(\frac{M}{M_{\odot}} \right)^{-1/2}, & \text{if } P \geq P_{\text{crit}} \\ -a_{\text{sat}} \left(\frac{P}{1 \text{ d}} \right)^{-1} \left(\frac{P_{\text{crit}}}{1 \text{ d}} \right)^{-2} \left(\frac{R}{R_{\odot}} \right)^{1/2} \left(\frac{M}{M_{\odot}} \right)^{-1/2}, & \text{if } P < P_{\text{crit}} \end{cases} \quad (8)$$

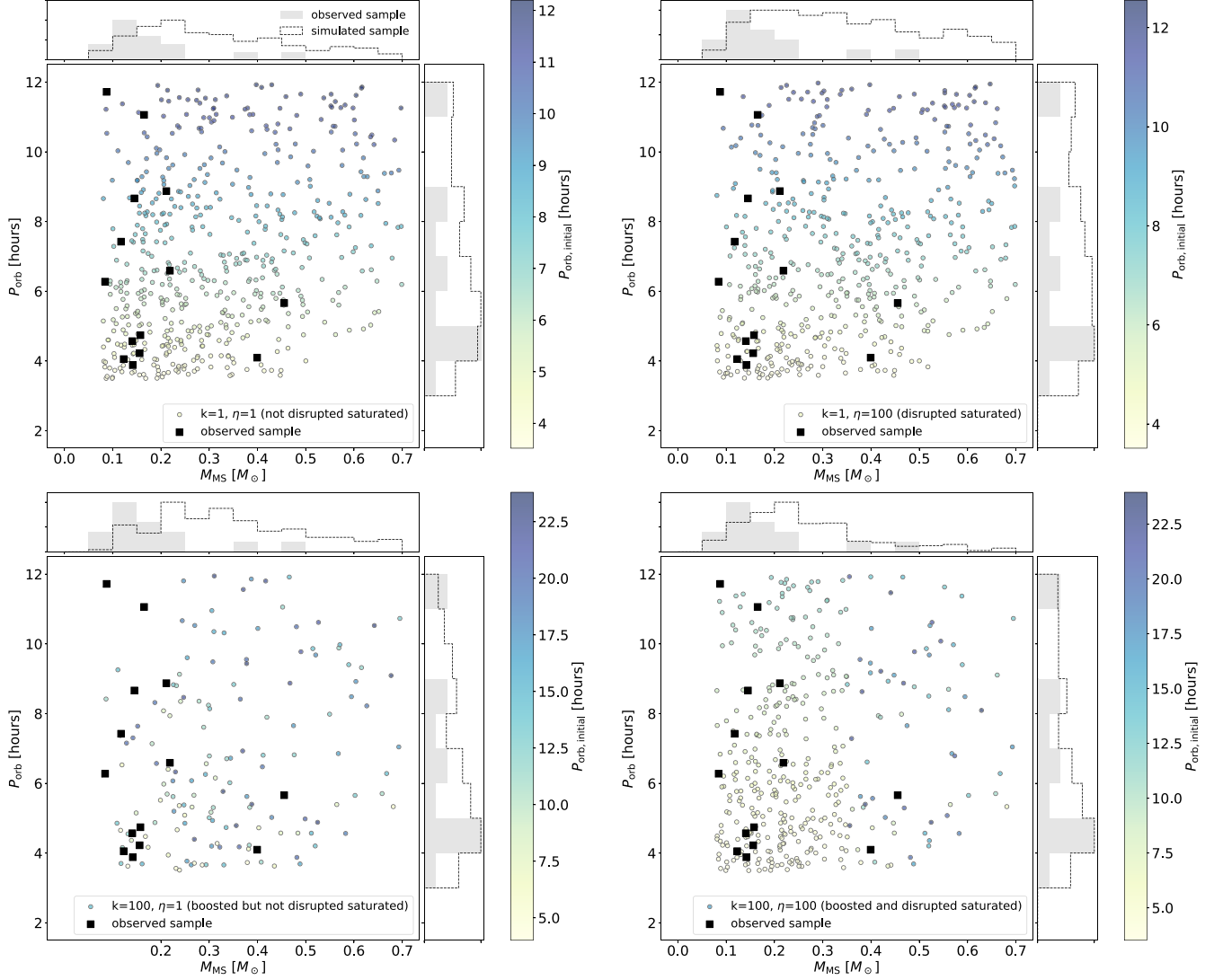


Figure 11. Results of our simulations for a population of sdB + MS binaries evolved under the saturated MB prescription (Equation (D3)). The boosted and disrupted model ($k = 100$, $\eta = 100$) matches the observed population best. The fiducial RVJ model predicts little period evolution within 100 Myr, and thus too many companions with $M_{\text{MS}} > 0.35M_{\odot}$.

where $a_{\text{sat}} = 1.04 \times 10^{35}$ erg (Sills et al. 2000). For the period range of interest, all simulated binaries have periods well below the saturation boundary P_{crit} ; therefore, we use the second equation given in Equation (8) for our analysis. Again, we introduce the following parameters k and η that control the strength of MB:

$$\dot{J} = \begin{cases} k\dot{J}_{\text{sat}}, & M_{\text{MS}} > 0.35M_{\odot} \\ \frac{k}{\eta}\dot{J}_{\text{sat}}, & M_{\text{MS}} < 0.35M_{\odot} \end{cases} \quad (9)$$

We can again solve for an analytical solution (see Appendix D.2). We repeat the same analysis as in Figure 10, now using the saturated MB law. The results of our simulation

are compared to the observed sdB + MS population in Figure 11.

Similar to the RVJ prescription, our simulated population best matches our observed population for boosted and disrupted ($k = 100$, $\eta = 100$) saturated MB. We selected the value of the boost parameter k by comparing the simulated population for various values (i.e., $k = 10, 20, 50, 75, 100$) against the observed sample and choosing the value that best matches the relative drop off we see toward high M_{MS} . We chose η to be equal to k .

We again use a two-sample KS test to compare the observed and simulated populations. We find a p-value of $\sim 1\%$ for the boosted and disrupted model with $k \gtrsim 100$ and $\eta \gtrsim 100$ whereas for the other three models, we find p-values of 0.01%–0.05%. The small size of our observed sample prevents us from being

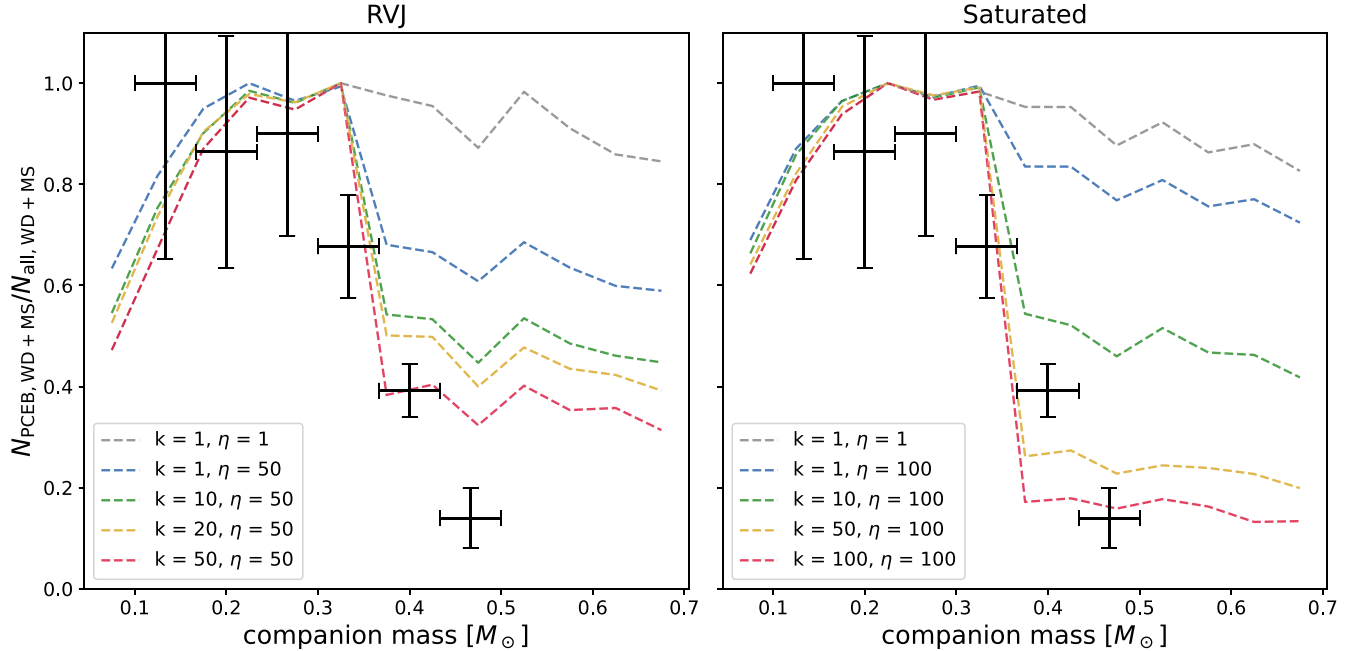


Figure 12. Predicted and observed WD + MS PCEB fractions for a range of MB laws. The observed fractions (black points) are taken from Schreiber et al. (2010), while dashed lines show population synthesis models described in the text. Different colors show different values of k and η . Both the observed and simulated samples are normalized to a maximum value of 1. As for the sdB + MS binaries, we find that—if the observed dearth of higher-mass companions is a result of MB—both disruption and boosting of MB above the fully convective limit are required to match observations.

able to place a tight upper limit on k , but we can rule out $k \gtrsim 300$, because in this case the simulations predict too few surviving PCEBs with MS companions above the fully convective limit. Again, here we remain agnostic about the physical origin of this stronger MB (see Section 6 for further discussion).

The period distributions of the simulated populations for all four variations are fairly uniform, similar to the results from the RVJ MB prescription.

5.3. Simulating Magnetic Braking for WD + MS PCEBs

We carried out similar simulations to model the evolution of short-period WD + MS PCEBs. We used the same initial period, eccentricity, and mass distribution models as in Section 5.1 but instead targeted systems containing He or CO WDs ($k_{\text{star}_1} = 10$ or 11), without a cut on WD mass. We considered all binaries that have undergone a common envelope event and applied MB using the same models we used for sdB + MS binaries. Since we expect WD + MS PCEBs to have a typical observable life time of ~ 1 Gyr, we choose the evolution time by randomly selecting an age for each system from $\mathcal{U}(0, 2)$ Gyr. We considered as PCEBs all systems with final periods below 4 days, roughly corresponding to the period range below which they would have been recognized as PCEBs with low-resolution spectroscopy (Schreiber et al. 2010).

Figure 12 compares our simulated results to the observed WD + MS population from SDSS as reported by

Schreiber et al. (2010). Following Schreiber et al. (2010), we normalize the observed sample of WD + MS population by plotting the ratio of PCEBs to all WD + MS binaries. For the observed sample from SDSS, we take $N_{\text{WD}+\text{MS},\text{all}}$ to be the number of all systems reported in the Schreiber et al. (2010) catalog. For our simulated sample, we take $N_{\text{WD}+\text{MS},\text{all}}$ to be the number of all WD + MS binaries, including PCEBs and systems that have not undergone a common envelope event. We chose this normalization to keep consistent with Belloni et al. (2024), who conducted a similar experiment. The left panel of Figure 12 shows results for the RVJ MB model, and the right panel shows results for the saturated MB model. The different colored dashed lines show predictions for different k and η . Similarly to the sdB + MS simulations, boosted MB ($k \gtrsim 50$) coupled with strong disruption ($\eta \approx 50\text{--}100$) below the fully convective boundary is required to match the observed population. Even for the RVJ prescription, models with disruption and no boosting predict a weaker drop-off above the fully convective boundary than is observed.

Our results are in agreement with findings from Belloni et al. (2024), confirming that our modeling of MB and the synthesis of the zero-age PCEBs are consistent with their study.

6. Summary and Discussion

In order to constrain the companion mass distribution of post-common envelope sdB + MS binaries, we carried out a

multi-epoch spectroscopic survey of bright, eclipsing systems. Our main results are as follows:

- (i) *Sample selection.* We selected 14 eclipsing sdB + MS systems with $3.8 \leq P_{\text{orb}} \leq 12$ hr and apparent magnitude $G < 16$ mag from the list of eclipsing sdB + MS systems reported in Schaffenroth et al. (2022) (Figure 2). We measured the orbital periods from their light curves (Figure 1). Our sample is $\sim 87\%$ complete with respect to the Geier (2020) sample in this period and apparent magnitude range and the selection function of our search is straightforward to model. Compared to previous work, our sample contains more long-period binaries (Figure 6). This is critical for measuring the companion mass distribution, because shorter-period binaries can only accommodate low-mass companions.
- (ii) *RV follow-up.* We conducted multi-epoch spectroscopic follow-up to measure the RVs of the sdB stars in our sample over the course of multiple nights (Figure 3). The ephemerides measured from the light curves allow us to constrain the sdB RV curves using only a few RV measurements (Figure 4). Then, assuming a typical mass for the sdB star and an inclination range informed by the fact that the binaries are eclipsing, we constrained the companion masses (Figures 5 and 6).
- (iii) *Companion mass distribution.* Our sample contains companion masses ranging from near the hydrogen burning limit to $0.45 M_{\odot}$, including the two most massive MS companions in HW Vir binaries discovered so far. The companion mass distribution peaks near $M_{\text{MS}} \sim 0.15 M_{\odot}$ and exhibits a drop off in a number of systems near $M_{\text{MS}} \sim 0.25\text{--}0.30 M_{\odot}$, slightly below the fully convective limit (Figure 6). The distribution is similar to what other studies have found for shorter period systems (Figure 6). We see no correlation between P_{orb} and M_{MS} .
- (iv) *Comparison to binary population models.* We created a synthetic population of zero-age sdB + MS PCEBs using COSMIC. We then evolved the population under various MB prescriptions by using the analytical solution of the period evolution, and mock observed this simulated population. Comparing this simulated sdB + MS population to our observed sample, we find that disrupted of MB, if coupled with boosted MB at higher masses, could explain the observed companion mass distribution (Figures 10 and 11). This is consistent with the findings by Belloni et al. (2024), where they conducted a similar experiment with a WD + MS population. There are higher mass WD companions to sdBs in the same period range as our sample, which suggests that it is unlikely for the observed distribution to be set by common envelope alone (Figure 8).

Most MB models in the literature, including the RVJ and saturated models we explored, were derived from empirical models of the rotation evolution of single stars. It is possible that MB in close binaries removes more angular momentum than MB in single stars with the same rotation periods.

One possibility is that irradiation of the MS star by its sdB companion boosts MB. Irradiation from the sdB will heat the atmosphere of the MS star, potentially leading to enhanced loss of mass and angular momentum. This may lead to significantly stronger MB in sdB + MS binaries than in single stars or MS + MS binaries, since the MS stars in sdB + MS binaries are more strongly irradiated than those in most other classes of close binaries. However, we also find that some boosting of MB is required to match the companion mass distribution of WD + MS binaries (Figure 12), which experience less irradiation.

Various previous works (e.g., Rappaport et al. 1983; Spruit & Ritter 1983; Howell et al. 2001; Schreiber et al. 2010; Knigge et al. 2011) have predicted that MB weakens or turns off below the fully convective boundary. Our data exhibits a drop off in the companion mass distribution near $\sim 0.2 M_{\odot}$, which could be explained by a disruption in MB for low-mass MS stars. However, comparing our observed sample to the population of WD + MS PCEBs, we find that sdB + MS systems cluster toward lower masses ($M_{\text{MS}} \sim 0.1\text{--}0.2 M_{\odot}$) compared to WD + MS systems ($M_{\text{MS}} \sim 0.1\text{--}0.4 M_{\odot}$), suggesting that the disruption of MB occurs at different masses for these two binaries (Figure 8).

If the weakening of MB below the fully convective boundary is gradual rather than abrupt, this might explain why sdB + MS binaries—which are subject to stronger irradiation-driven mass loss—contain few MS stars above $\sim 0.2 M_{\odot}$. Given that evidence for disruption is observed at different masses for the two types of PCEBs, this could imply that disruption is driven by binary interactions not accounted for in standard MB models, such as e.g., interaction between the magnetic fields of the two component stars.

Our study is in agreement with findings from Belloni et al. (2024) and provides additional support for boosted and disrupted MB in PCEBs, if we assume that MB is the dominant contributing factor to angular momentum loss and period evolution of PCEBs. However, there is not yet a concrete physical explanation for the boosting and disruption of MB that we infer, and there may be other processes that contribute to the period evolution of these systems. Further investigation is necessary to understand the underlying mechanisms that results in this boosting and disruption.

An alternative explanation for the lack of higher-mass companions in post-common envelope sdB binaries could be that more massive companions go through stable mass transfer instead, and thus end up at long orbital periods. This possibility seems unlikely, however, because there are plenty of post-common envelope sdB+WD binaries in short-period orbits containing WDs with masses near $0.6 M_{\odot}$. And indeed, most of

the known post-stable mass transfer sdB + MS binaries contain MS stars with $M_{\text{MS}} \gtrsim 0.8 M_{\odot}$ (e.g., Vos et al. 2018).

Acknowledgments

We thank the referee for their constructive comments. We also thank Jim Fuller and Stefan Geier for helpful discussions. The Kavli Institute for Theoretical Physics (KITP) hosted the program, “White Dwarfs as Probes of the Evolution of Planets, Stars, the Milky Way, and the Expanding Universe,” during which this project was initiated.

This research was supported in part by the U.S. National Science Foundation (NSF) grant AST-2307232, and in part by grants PHY-1748958 and AST-2107070.

This work has made use of data from the European Space Agency (ESA) mission Gaia (<https://www.cosmos.esa.int/gaia>), processed by the Gaia Data Processing and Analysis Consortium (DPAC, <https://www.cosmos.esa.int/web/gaia/dpac/consortium>). Funding for the DPAC has been provided by national institutions, in particular the institutions participating in the Gaia Multilateral Agreement.

This work is based in part on observations obtained with the Samuel Oschin 48 inch Telescope at the Palomar Observatory as part of the Zwicky Transient Facility project. ZTF is supported by the NSF under grant AST-1440341 and a collaboration including Caltech, IPAC, the Weizmann Institute for Science, the Oskar Klein Center at Stockholm University, the University of Maryland, the University of Washington, Deutsches Elektronen-Synchrotron and Humboldt University, Los Alamos National Laboratories, the TANGO Consortium of Taiwan, the University of Wisconsin at Milwaukee, and the Lawrence Berkeley National Laboratory. Operations are conducted by the Caltech Optical Observatories (COO), the Infrared Processing and Analysis Center (IPAC), and the University of Washington (UW).

Some of the data presented herein were obtained at Keck Observatory, which is a private 501(c)3 non-profit organization operated as a scientific partnership among the California Institute of Technology, the University of California, and the National Aeronautics and Space Administration. The Observatory was made possible by the generous financial support of the W. M. Keck Foundation.

Software: Astropy (Astropy Collaboration et al. 2013, 2018, 2022), COSMIC (Breivik et al. 2020).

Appendix A Radial Velocities

Table of all radial velocities measured by spectroscopic follow-up, their observation time and the instrument used.

Table 4
All measured RVs

Object Name	Observation Time (HJD)	Radial Velocity (km s ⁻¹)	Instrument
J1533+3759	2460055.7312	60 ± 10	DBSP
J1533+3759	2460055.8064	-84 ± 10	DBSP
J1533+3759	2460055.8902	58 ± 10	DBSP
J1533+3759	2460055.9792	-69 ± 10	DBSP
J1533+3759	2460344.0607	-53 ± 5	ESI
J1533+3759	2460344.0649	-58 ± 5	ESI
J1533+3759	2460344.1242	26 ± 5	ESI
J1533+3759	2460344.1553	78 ± 5	ESI
J1920+3722	2460056.0040	-60 ± 10	DBSP
J1920+3722	2460055.9193	55 ± 10	DBSP
J1920+3722	2460438.7822	85 ± 10	DBSP
J1920+3722	2460463.9611	63 ± 5	ESI
J1920+3722	2460464.0117	-37 ± 5	ESI
J0557-1409	2459905.9428	179 ± 10	DBSP
J0557-1409	2459914.0126	28 ± 10	DBSP
J0557-1409	2460201.0031	-89 ± 10	DBSP
J0557-1409	2460202.0067	-97 ± 10	DBSP
J0557-1409	2460264.9379	113 ± 5	ESI
J0557-1409	2460265.0220	-56 ± 5	ESI
J0557-1409	2460284.8363	-43 ± 10	DBSP
J0557-1409	2460284.9071	107 ± 10	DBSP
J0619-1417	2459906.0087	0 ± 10	DBSP
J0619-1417	2459914.0063	151 ± 10	DBSP
J0619-1417	2460264.9434	113 ± 5	ESI
J0619-1417	2460265.0270	73 ± 5	ESI
J0619-1417	2460265.0531	21 ± 5	ESI
J0619-1417	2460284.8454	112 ± 10	DBSP
J0619-1417	2460284.9152	58 ± 10	DBSP
J1852+1445	2459899.7008	22 ± 10	LRIS
J1852+1445	2459905.5994	-4 ± 10	DBSP
J1852+1445	2459913.5755	-40 ± 10	DBSP
J1852+1445	2460055.9488	32 ± 10	DBSP
J1852+1445	2460200.6407	75 ± 10	DBSP
J1852+1445	2460200.7065	-32 ± 10	DBSP
J1852+1445	2460225.7755	93 ± 10	LRIS
J1831+1345	2459913.5906	-94 ± 10	DBSP
J1831+1345	2460055.8568	-98 ± 10	DBSP
J1831+1345	2460055.9301	46 ± 10	DBSP
J1831+1345	2460344.1721	-9 ± 5	ESI
J2240+5437	2459899.7947	-155 ± 10	LRIS
J2240+5437	2459899.9316	108 ± 10	LRIS
J2240+5437	2460200.6566	163 ± 10	DBSP
J2240+5437	2460200.7149	-34 ± 10	DBSP
J2240+5437	2460284.5866	86 ± 10	DBSP
J0519-1916	2459900.0532	-73 ± 10	LRIS
J0519-1916	2459905.9520	78 ± 10	DBSP
J0519-1916	2459915.5922	39.48 ± 5	FEROS
J0519-1916	2459916.6030	59.40 ± 5	FEROS
J0519-1916	2459917.5771	-78.84 ± 5	FEROS
J0519-1916	2459919.5742	-36.88 ± 5	FEROS
J0519-1916	2459920.6471	-87.63 ± 5	FEROS
J0519-1916	2460264.9327	-73 ± 5	ESI
J0519-1916	2460265.0728	68 ± 5	ESI
J0519-1916	2460284.8283	58 ± 10	DBSP
J0519-1916	2460284.9003	20 ± 10	DBSP
J1630+1801	2460055.8497	-109 ± 10	DBSP
J1630+1801	2460055.9978	2 ± 10	DBSP
J1630+1801	2460344.1483	-73 ± 5	ESI

Table 4
(Continued)

Object Name	Observation Time (HJD)	Radial Velocity (km s ⁻¹)	Instrument
J1802-5532	2460374.8937	-21 ± 5	FEROS
J1802-5532	2460375.8840	-98 ± 5	FEROS
J1802-5532	2460376.8899	-104 ± 5	FEROS
J0808+3202	2459905.9611	108 ± 10	DBSP
J0808+3202	2459914.0181	28 ± 10	DBSP
J0808+3202	2459914.0642	114 ± 10	DBSP
J0808+3202	2460201.0083	102 ± 10	DBSP
J0808+3202	2460201.0121	84 ± 10	DBSP
J0808+3202	2460202.0266	48 ± 10	DBSP
J0808+3202	2460264.9680	106 ± 5	ESI
J0808+3202	2460265.0583	22 ± 5	ESI
J0808+3202	2460343.9595	-2 ± 5	ESI
J0808+3202	2460344.0580	92 ± 5	ESI
J0808+3202	2460344.0538	103 ± 5	ESI
J0241-6855	2459912.5673	111.00 ± 5	FEROS
J0241-6855	2459912.6816	28.26 ± 5	FEROS
J0241-6855	2459914.6449	-1.35 ± 5	FEROS
J0241-6855	2459914.7741	80.22 ± 5	FEROS
J0612-1740	2459914.8046	-72.09 ± 5	FEROS
J0612-1740	2459914.6796	-14.25 ± 5	FEROS
J0612-1740	2459916.5266	-9.03 ± 5	FEROS
J0612-1740	2459917.6901	-55.11 ± 5	FEROS
J0612-1740	2459919.5994	-38.82 ± 5	FEROS
J0612-1740	2459920.6471	-68.13 ± 5	FEROS
J0612-1740	2460284.8519	-17 ± 10	DBSP
J0612-1740	2460284.9216	-82 ± 10	DBSP

Appendix B

Companion Masses for High- and Low-mass sdBs

In our fiducial analysis, we assume sdB masses of $(0.45\text{--}0.55)M_{\odot}$. Although we expect the majority of observed sdBs fall in this mass range, theory predicts the existence of both higher-mass ($M_{\text{sdB}} \sim 0.60M_{\odot}$) and lower-mass ($M_{\text{sdB}} \sim 0.35M_{\odot}$) sdBs. Here we test the sensitivity of our results to the assumed sdB mass. We repeated the analysis in Section 4.3 but assume $M_{\text{sdB}} = 0.35M_{\odot}$ and $M_{\text{sdB}} = 0.60M_{\odot}$. The inferred companion mass limits are shown with triangles in Figure 13. Although these limits span a wider range than the uncertainties reported in Table 3, the inferred companion mass ranges are still broadly similar to our fiducial constraints and do not move any companions above or below the fully convective limit. We also stress that we do expect most systems in our sample to have $0.45 < M_{\text{sdB}}/M_{\odot} < 0.55$; the limits in Figure 13 represent extreme cases.

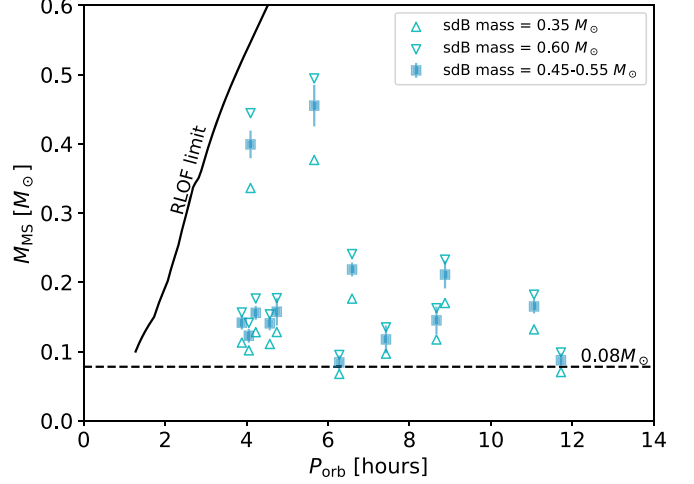


Figure 13. Companion mass vs. orbital period. Dashed line marks the hydrogen burning limit; solid line shows where a MS companion would overflow its Roche lobe. Square points with error bars show the fiducial inferred companion masses assuming $M_{\text{sdB}} = (0.45\text{--}0.55)M_{\odot}$. Triangles show upper and lower limits inferred for $M_{\text{sdB}} = 0.60M_{\odot}$ and $M_{\text{sdB}} = 0.35M_{\odot}$, respectively. These more generous limits lead to broader ranges of dynamically allowed M_{MS} but qualitatively consistent results; e.g., even if all sdBs in our sample had $M_{\text{sdB}} = 0.6M_{\odot}$, 85% of the companions would still have $M_{\text{MS}} < 0.25M_{\odot}$.

Appendix C

Selection Function

Selection function used to mock-observe the simulated population. We impose bounds on the population's orbital period and select based on the eclipse probability of the systems. From geometry of binaries alone, for randomly oriented orbits, the eclipse probability is given by:

$$p = \frac{R_{\text{sdB}} + R_{\text{MS}}}{a}, \quad (\text{C1})$$

where a is the semimajor axis of the orbit, and R_{sdB} and R_{MS} are the radii of the sdB and the companion MS star, respectively.

We use the definition of self-gravitation to define the mass–radius relation for the sdB ($R_{\text{sdB}} = \sqrt{GM_{\text{sdB}}/g_{\text{sdB}}}$) and take a typical value of $\log(g_{\text{sdB}}/[\text{cm s}^{-2}]) = 5.5$. R_{MS} is set by the mass–radius relation from isochrones (Choi et al. 2016).

$$p = \left[\frac{4\pi^2}{GM_{\odot}(M_{\text{sdB}} + M_{\text{ms}})P_{\text{orb}}^2} \right]^{1/3} \left[R_{\text{MS}} + \sqrt{\frac{GM_{\odot}M_{\text{sdB}}}{g_{\text{sdB}}}} \right] \quad (\text{C2})$$

With the above eclipse probability, the selection function is given as:

$$\begin{cases} 3.8 \leq P_{\text{orb}} \leq 12 \text{ hr} \\ p = \left[\frac{4\pi^2}{GM_{\odot}(M_{\text{sdb}} + M_{\text{MS}})P^2} \right]^{1/3} \left[R_{\text{MS}} + \sqrt{\frac{GM_{\odot}M_{\text{sdb}}}{g_{\text{sdb}}}} \right] \leq \mathcal{U}(0, 1) \end{cases} \quad (\text{C3})$$

Appendix D Magnetic Braking Analytical Models

We solve for the orbital period evolution of a sdB + MS binary using a similar methods as outlined in El-Badry et al. (2022). Only the MS star experiences MB, and we assume no mass loss and total tidally locking.

D.1. RVJ Magnetic Braking Prescription

The analytical solution for orbital period evolution under the RVJ MB prescription:

$$P_{\text{orb}}(t) = \begin{cases} \left[P_{\text{orb},0}^{10/3} - \frac{k}{\eta} \frac{10R_{\text{MS}}^4(q+1)^{1/3}}{qM_{\text{MS}}^{2/3}} t \right]^{3/10} & M_{\text{MS}} < 0.35M_{\odot} \\ \left[P_{\text{orb},0}^{10/3} - k \frac{10R_{\text{MS}}^4(q+1)^{1/3}}{qM_{\text{MS}}^{2/3}} t \right]^{3/10} & M_{\text{MS}} > 0.35M_{\odot} \end{cases} \quad (\text{D1})$$

where $P_{\text{orb},0}$ is the initial period of the system (i.e., P_{orb} of the zero-age PCEB) in days, R_{MS} is the radius of the companion in solar radii, and $q = M_{\text{sdb}}/M_{\text{MS}}$. t is a dimensionless time defined as $t = T/T_{\text{RVJ}}$ where T is the age of the star where we take the age of the star right after the common envelope ejection to be $T = 0$, and

$$T_{\text{RVJ}} = (1 \text{ day})^{1/3} M_{\odot}^{5/3} \left(\frac{G^2}{2\pi} \right)^{1/3} a_{\text{RVJ}}^{-1} \approx 5.8 \text{ Gyr}. \quad (\text{D2})$$

Here k and η are introduced to allow us to parameterize the “boost” and the “disruption” of the MB prescriptions as described in the main text of the paper.

D.2. Saturated Magnetic Braking Prescription

We carry out a similar calculation for the saturated MB prescription, and solve for the analytical solution of P_{orb} :

$$P_{\text{orb}}(t) = \begin{cases} \left[P_{\text{orb},0}^{4/3} - \frac{k}{\eta} \frac{4R_{\text{MS}}^{1/2}(q+1)^{1/3}}{qM_{\text{MS}}^{13/6}} t \right]^{3/4} & M_{\text{MS}} < 0.35M_{\odot} \\ \left[P_{\text{orb},0}^{4/3} - k \frac{4R_{\text{MS}}^{1/2}(q+1)^{1/3}}{qM_{\text{MS}}^{13/6}} t \right]^{3/4} & M_{\text{MS}} > 0.35M_{\odot} \end{cases} \quad (\text{D3})$$

t is again a dimensionless time defined as $t = T/T_{\text{sat}}$ where T_{sat} is defined as:

$$T_{\text{sat}} = \frac{(1 \text{ day})^{4/3} M_{\odot}^{5/3} G^{2/3}}{(2\pi)^{4/3} K_W \omega_{\text{crit},1}^2} \quad (\text{D4})$$

where $K_W = 2.7 \times 10^{47} \text{ g cm}^2$ (Sills et al. 2000).

Appendix E Variations on the Magnetic Braking Simulations

E.1. PCEBs Hosting Low-mass sDBs

Our analysis in Section 5 selects binaries hosting $0.4\text{--}0.5 M_{\odot}$ He WDs as representative of sDBs formed through the canonical channel. This selection is likely inappropriate for lower-mass sDBs formed from $\sim 2 M_{\odot}$ progenitors that ignited helium burning when their cores were non-degenerate (e.g., Han et al. 2002). We investigate predictions for lower-mass sDBs in Figure 14, where we compare the observed population to COSMIC simulations with initial $M_1 > 2 M_{\odot}$ that form He WDs with mass $0.30\text{--}0.40 M_{\odot}$. Compared to our fiducial simulations, the PCEB population predicted in this case is heavily biased toward high-mass companions, with few binaries predicted to have $M_{\text{MS}} < 0.15 M_{\odot}$ and less overlap with the observed population. COSMIC predicts low-mass companions that enter a

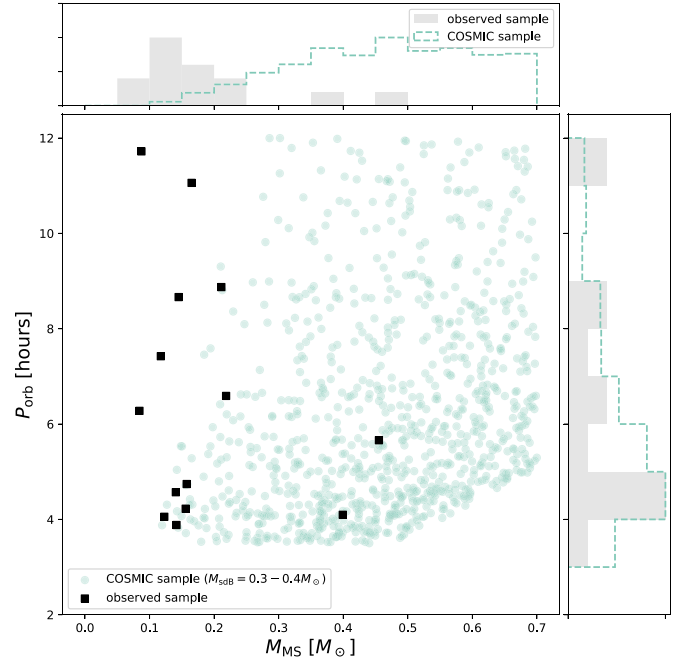


Figure 14. Synthetic zero-age sdB + MS PCEB population predicted by COSMIC for binaries with WD mass $M_{\text{WD}} = 0.3\text{--}0.4 M_{\odot}$ (compare to Figure 9). Black squares show our observed sample. The predicted PCEB population is heavily biased toward higher-mass companions, because would-be PCEBs with lower-mass companions are predicted to merge.

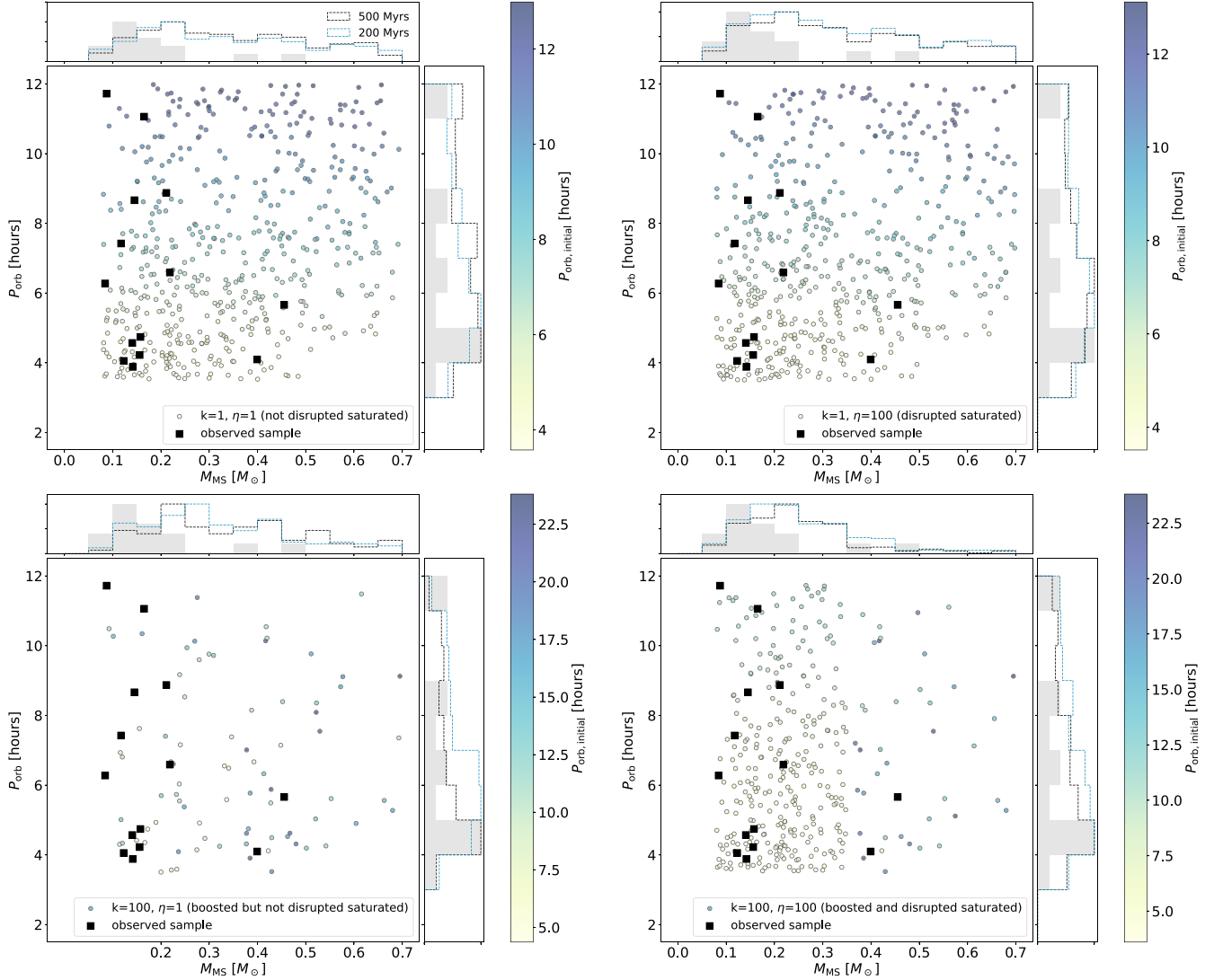


Figure 15. Simulations of a population of sdB + MS binaries evolved under the saturated MB prescription (Equation (8)). Black points show our observed sample. Colored points show a predicted PCEB population from COSMIC evolved for $\mathcal{U}(0, 500)$ Myr according to Equation (D3) and selected to be eclipsing. The dotted black line in the histogram represents the population which has been evolved for $\mathcal{U}(0, 500)$ Myr and the blue line represents the population which has been evolved for $\mathcal{U}(0, 200)$ Myr, as assumed in our fiducial model. All histograms are normalized by their tallest bin. There is little difference in the companion mass distributions predicted between the two age distributions.




common envelope with a star low on the giant branch—as is required to form a low-mass WD or sdB—will not survive, because they lack the orbital energy required to eject the giant’s envelope. For this reason, we restrict our analysis in the main text to PCEBs with $0.4\text{--}0.5M_{\odot}$ He WDs.

E.2. Sensitivity to the Assumed sdB Lifetime

In Section 5.2.2, we assume that sdBs have a lifetime of 200 Myr. Although this is reasonable for typical sdBs, the He burning lifetime of lower-mass sdBs ($M_{\text{sdB}} \sim 0.35M_{\odot}$) can be longer, up to 500 Myr. To test the sensitivity of our results to the

assumed sdB lifetime, we repeat the same analysis but with an evolution time drawn from $\mathcal{U}(0, 500)$ Myr. The results are shown in Figure 15. The population evolved for $\mathcal{U}(0, 200)$ Myr and $\mathcal{U}(0, 500)$ Myr have similar companion mass distributions, suggesting the simulations are insensitive to the assumed sdB lifetime.

ORCID iDs

Lisa Blomberg  <https://orcid.org/0009-0004-4475-2121>
 Pranav Nagarajan  <https://orcid.org/0000-0002-1386-0603>
 Natsuko Yamaguchi  <https://orcid.org/0000-0001-6970-1014>

References

- Astropy Collaboration, Price-Whelan, A. M., Lim, P. L., et al. 2022, *ApJ*, **935**, 167
- Astropy Collaboration, Price-Whelan, A. M., Sipösrccz, B. M., et al. 2018, *AJ*, **156**, 123
- Astropy Collaboration, Robitaille, T. P., Tollerud, E. J., et al. 2013, *A&A*, **558**, A33
- Bellm, E. C., Kulkarni, S. R., Graham, M. J., et al. 2019, *PASP*, **131**, 018002
- Belloni, D., Schreiber, M. R., Moe, M., El-Badry, K., & Shen, K. J. 2024, *A&A*, **682**, A33
- Bouma, L. G., Palumbo, E. K., & Hillenbrand, L. A. 2023, *ApJL*, **947**, L3
- Brahm, R., Jordán, A., & Espinoza, N. 2017, *PASP*, **129**, 034002
- Breivik, K., Coughlin, S., Zevin, M., et al. 2020, *ApJ*, **898**, 71
- Breivik, K., Coughlin, S., Zevin, M., et al. 2021, COSMIC: Compact Object Synthesis and Monte Carlo Investigation Code, Astrophysics Source Code Library, ascl:2108.022
- Brown, T. M. 2014, *ApJ*, **789**, 101
- Chaboyer, B., Demarque, P., & Pinsonneault, M. H. 1995, *ApJ*, **441**, 865
- Choi, J., Dotter, A., Conroy, C., et al. 2016, *ApJ*, **823**, 102
- Dorman, B., Rood, R. T., & O'Connell, R. W. 1993, *ApJ*, **419**, 596
- El-Badry, K., Conroy, C., Fuller, J., et al. 2022, *MNRAS*, **517**, 4916
- Foreman-Mackey, D., Hogg, D. W., Lang, D., & Goodman, J. 2013, *PASP*, **125**, 306312
- Gaia Collaboration, Vallenari, A., Brown, A. G. A., et al. 2023, *A&A*, **674**, A1
- Geier, S. 2020, *A&A*, **635**, A193
- Green, G. M., Schlafly, E., Zucker, C., Speagle, J. S., & Finkbeiner, D. 2019, *ApJ*, **887**, 93
- Han, Z., Podsiadlowski, P., Maxted, P. F. L., & Marsh, T. R. 2003, *MNRAS*, **341**, 669
- Han, Z., Podsiadlowski, P., Maxted, P. F. L., Marsh, T. R., & Ivanova, N. 2002, *MNRAS*, **336**, 449
- Heber, U. 2016, *PASP*, **128**, 082001
- Howell, S. B., Nelson, L. A., & Rappaport, S. 2001, *ApJ*, **550**, 897
- Hubeny, I., & Lanz, T. 2017, arXiv:1706.01859
- Hurley, J. R., Tout, C. A., & Pols, O. R. 2002, *MNRAS*, **329**, 897
- Kaufer, A., Stahl, O., Tubbesing, S., et al. 1999, *Msngr*, **95**, 8
- Kawaler, S. D. 1988, *ApJ*, **333**, 236
- Knigge, C., Baraffe, I., & Patterson, J. 2011, *ApJS*, **194**, 28
- Kochanek, C. S., Shappee, B. J., Stanek, K. Z., et al. 2017, *PASP*, **129**, 104502
- Kroupa, P. 2001, *MNRAS*, **322**, 231
- Kruckow, M. U., Neunteufel, P. G., Di Stefano, R., Gao, Y., & Kobayashi, C. 2021, *ApJ*, **920**, 86
- Kupfer, T., Geier, S., Heber, U., et al. 2015, *A&A*, **576**, A44
- Lallement, R., Vergely, J. L., Babusiaux, C., & Cox, N. L. J. 2022, *A&A*, **661**, A147
- Lei, Z., Zhao, J., Németh, P., & Zhao, G. 2020, *ApJ*, **889**, 117
- Lomb, N. R. 1976, *Ap&SS*, **39**, 447
- Lu, Y. L., See, V., Amard, L., Angus, R., & Matt, S. P. 2024, *NatAs*, **8**, 223
- Ma, L., & Fuller, J. 2024, Tidal Spin-up of Subdwarf B Stars, *ApJ*, **975**, 1
- Matt, S. P., Brun, A. S., Baraffe, I., Bouvier, J., & Chabrier, G. 2015, *ApJL*, **799**, L23
- Maxted, P. F. L. 2016, *A&A*, **591**, A111
- Mestel, L. 1968, *MNRAS*, **138**, 359
- Mestel, L., & Spruit, H. C. 1987, *MNRAS*, **226**, 57
- Nagarajan, P., El-Badry, K., van Rodriguez, A. C., & Roulston, B. 2023, *MNRAS*, **524**, 4367
- Nemeth, P., Östensen, R., Tremblay, P.-E., & Hubeny, I. 2014, in ASP Conf. Ser. 481, 6th Meeting on Hot Subdwarf Stars and Related Objects, ed. V. van Grootel et al. (San Francisco, CA: ASP), 95
- Newton, E. R., Irwin, J., Charbonneau, D., et al. 2016, *ApJ*, **821**, 93
- Oke, J. B., Cohen, J. G., Carr, M., et al. 1994, *Proc. SPIE*, **2198**, 178
- Oke, J. B., & Gunn, J. E. 1982, *PASP*, **94**, 586
- Pecaut, M. J., & Mamajek, E. E. 2013, *ApJS*, **208**, 9
- Perley, D. A. 2019, *PASP*, **131**, 084503
- Politano, M., & Weiler, K. P. 2006, *ApJL*, **641**, L137
- Preece, H. P., Tout, C. A., & Jeffery, C. S. 2018, *MNRAS*, **481**, 715
- Prochaska, J., Hennawi, J., Westfall, K., et al. 2020, *JOSS*, **5**, 2308
- Raghavan, D., McAlister, H. A., Henry, T. J., et al. 2010, *ApJS*, **190**, 1
- Rappaport, S., Verbunt, F., & Joss, P. C. 1983, *ApJ*, **275**, 713
- Rebassa-Mansergas, A., Gänsicke, B. T., Schreiber, M. R., et al. 2018, *MNRAS*, **402**, 620
- Reiners, A., Basri, G., & Browning, M. 2009, *ApJ*, **692**, 538
- Ricker, G. R., Winn, J. N., Vanderspek, R., et al. 2015, *JATIS*, **1**, 014003
- Scargle, J. D. 1982, *ApJ*, **263**, 835
- Schaffenroth, V., Casewell, S. L., Schneider, D., et al. 2021, *MNRAS*, **501**, 3847
- Schaffenroth, V., Geier, S., Heber, U., et al. 2018, *A&A*, **614**, A77
- Schaffenroth, V., Pelisoli, I., Barlow, B. N., Geier, S., & Kupfer, T. 2022, *A&A*, **666**, A182
- Schatzman, E. 1962, *AnAp*, **25**, 18
- Schindler, J.-T., Green, E. M., & Arnett, W. D. 2015, *ApJ*, **806**, 178
- Schreiber, M. R., Gänsicke, B. T., Rebassa-Mansergas, A., et al. 2010, *A&A*, **513**, L7
- Sheinis, A. I., Bolte, M., Epps, H. W., et al. 2002, *PASP*, **114**, 851
- Sills, A., Pinsonneault, M. H., & Terndrup, D. M. 2000, *ApJ*, **534**, 335
- Skumanich, A. 1972, *ApJ*, **171**, 565
- Spruit, H. C., & Ritter, H. 1983, *A&A*, **124**, 267
- Verbunt, F., & Zwaan, C. 1981, *A&A*, **100**, L7
- Vos, J., Németh, P., Vučković, M., Østensen, R., & Parsons, S. 2018, *MNRAS*, **473**, 693
- Weber, E. J., & Davis, L., J. 1967, *ApJ*, **148**, 217
- Zahn, J. P. 1977, *A&A*, **57**, 383
- Zorotovic, M., Schreiber, M. R., Gänsicke, B. T., & Nebot Gómez-Morán, A. 2010, *A&A*, **520**, A86